Inter-annual and decadal tidal variability in the South China Sea using S_TIDE

Haidong Pan[1], Adam Thomas Devlin[2], and Xianqing Lv[3]

[1]Key Laboratory of Physical Oceanography (Ocean University of China)
[2]School of Geography and Environment, Jiangxi Normal University
[3]Physical Oceanography Laboratory, Qingdao Collaborative Innovation Center of Marine Science and Technology (CIMST), Ocean University of China, and Qingdao National Laboratory for Marine Science and Technology

November 23, 2022

Abstract

Understanding time-changing tidal characteristics is essential for numerous practical purposes, such as flood prevention, navigation, and ocean engineering. Previous studies mainly focus on tidal evolution in coastal areas while tidal changes in deep water areas receive limited attention due to the lack of long-term high-frequency sea level records. In this paper, we extract the inter-annual and decadal tidal variability in the South China Sea (SCS) from 24 coastal tide gauges and 25-year satellite altimeter observations using the novel S_TIDE toolbox. Through numerous sensitivity experiments, it is found that ˜17 independent points (IPs) are suitable for extracting inter-annual and decadal tidal variability in the deep basin of the SCS. It is also found that tidal variability and sea level variability are closely correlated in most parts of the SCS. The high correlation between tidal variability and sea level variability in the central deep basin of the SCS is associated with the El Niño–Southern Oscillation(ENSO). The results obtained from satellite data are less stable and accurate than those obtained from long-term tidal gauge observations, but the methods described here provide a strong foundation for future research on time-varying tidal dynamics using the combination of tide gauges and satellite altimeter data.

Inter-annual and decadal tidal variability in the South China Sea using S_TIDE

Haidong Pan[1,2], Adam Thomas Devlin [3,4,5,*] , Xianqing Lv[1,2,*]

[1] *Key Laboratory of Physical Oceanography, Ocean University of China, Qingdao, China*

[2] *Qingdao National Laboratory for Marine Science and Technology, Qingdao, China*

[3] *Key Lab of Poyang Lake Wetland and Watershed Research of Ministry of Education, Nanchang 330022, China*

[4] *School of Geography and Environment, Jiangxi Normal University, Nanchang 330022, China*

[5] *The Chinese University of Hong Kong, Shatin, New Territories, Hong Kong SAR, China.*

**Corresponding author*

Email address: Adam T.Devlin (atdevin@jxnu.edu.cn)

Xianqing Lv (xqinglv@ouc.edu.cn)

To be submitted to JGR-Oceans

Key Points:

Inter-annual and decadal tidal variability in the South China Sea is extracted from satellite altimeter data for the first time.

Tidal variability and sea level variability are highly correlated in the South China Sea

Tidal dynamics are undergoing rapid changes in the central deep basin of the South China Sea

ABSTRACT

Understanding time-changing tidal characteristics is essential for numerous practical purposes, such as flood prevention, navigation, and ocean engineering. Previous studies mainly focus on tidal evolution in coastal areas while tidal changes in deep water areas receive limited attention due to the lack of long-term high-frequency sea level records. In this paper, we extract the inter-annual and decadal tidal variability in the South China Sea (SCS) from 24 coastal tide gauges and 25-year satellite altimeter observations using the novel S_TIDE toolbox. Through numerous sensitivity experiments, it is found that ~17 independent points (IPs) are suitable for extracting inter-annual and decadal tidal variability in the deep basin of the SCS. It is also found that tidal variability and sea level variability are closely correlated in most parts of the SCS. The high correlation between tidal variability and sea level variability in the central deep basin of the SCS is associated with the El Niño–Southern Oscillation (ENSO). The results obtained from satellite data are less stable and accurate than those obtained from long-term tidal gauge observations, but the methods described here provide a strong foundation for future research on time-varying tidal dynamics using the combination of tide gauges and satellite altimeter data.

Key words: tides, tidal variability, South China Sea, harmonic analysis, satellite altimeter data, sea level variability

1. Introduction

Ocean tides show obvious non-astronomical variations worldwide due to perturbations from factors such as river discharge (Matte et al., 2013, 2014; Pan and Lv, 2019), ice cover (Zhang et al., 2019), sea level rise (Pelling and Green, 2013) and water depth and shoreline change induced by human activities (Familkhalili and Talke, 2016; Chant et al., 2018; Ralston et al., 2019). Temporal changes of major tidal constituents have been reported at local or regional scales in the Hawaiian Islands (Ray and Mitchum, 1997; Mitchum and Chiswell, 2000; Colosi and Munk, 2006), the Gulf of Maine (Godin 1995; Ray, 2006; Pan et al., 2019), the Western Pacific (Devlin et al., 2014), the Eastern Pacific (Jay, 2009), the coast of China (Feng et al., 2015) and the North Atlantic (Ray, 2009; Muller, 2011).

Most previous studies have focused on tidal changes in coastal areas since nearly all tide gauges are located in these areas. However, tidal changes in the deep sea have received less attention due to the lack of long-term sea level observations. Since the launch of the TOPEX/Poseidon (T/P) mission in 1992 and the subsequent Jason series of altimetry platforms, satellite altimeter data have been widely used in numerous studies of tidal dynamics and have significantly enriched our knowledge of ocean tides in the deep sea. Satellite-derived tidal constants have been assimilated into tidal models which have significantly improved their accuracy (Stammer et al., 2014). However, to the best of our knowledge, no studies have thoroughly investigated tidal evolution or short-term tidal variability in the deep ocean using satellite altimeter data.

This may be due to the long sampling intervals required and the limitations of classical harmonic analysis (CHA).

CHA assumes that tides are effectively stationary, and that the amplitudes and phases of tidal constituents are completely predictable based on astronomy. Tidal constants can be obtained from hourly water level records observed at tide gauges by divided long-term records into shorter analysis windows (typically yearly or monthly), and performing harmonic analysis on each window. However, this is not suitable for satellite altimeter data due to the temporal coarseness of the observations. To adequately analyze T/P satellite data, at least 9.18-year observations are needed to fully resolve the eight largest tidal constituents (Ray 1998). Thus, results obtained by CHA can only obtain 9.18-year averaged tidal amplitudes and phases.

Continuous wavelet transform (CWT) and empirical mode decomposition (EMD) are powerful tools for non-stationary and nonlinear time series. They can resolve amplitudes in frequency and time domains simultaneously, though the resolution of constituents within a tidal band is limited (Matte et al., 2013; Pan et al., 2018a). Matte et al. (2013, 2014) developed the non-stationary tidal harmonic analysis tool NS_TIDE based on theoretical models of river tides. Although NS_TIDE has particularly good performance in tidal rivers, it cannot be applied to non-stationary tides that are influenced by other dynamical mechanisms (Pan et al., 2018b). Recently, Pan et al. (2018b) developed a novel non-stationary tidal analysis tool entitled S_TIDE based on enhanced harmonic analysis (EHA) proposed by Jin et al. (2018).

EHA assumes that tidal amplitudes and phases are time-varying and solves them based on an independent point (IP) scheme (Pan et al., 2017, 2018b). The S_TIDE MATLAB toolkit has been developed to explore river-tide interplay in Columbia River Estuary (Pan et al., 2018b), the temporal changes of M_2 nodal modulation in the Gulf of Maine (Pan et al., 2019) and the seasonal variations of major constituents in the Bohai Sea (Wang et al., 2020).

The purpose of this article is twofold: (1) to extract inter-annual and decadal variations of the amplitudes of major constituents in the South China Sea (SCS) from coastal tide gauges as well as satellite altimeter data using S_TIDE, and (2) to examine whether inter-annual and decadal tidal variability are correlated to sea level variability in the SCS using the tidal anomaly correlation (TAC) method. The reminder of this paper is structured as follows. The study area and data employed are described in section 2. Methodologies including EHA and TAC are detailed in section 3. Section 4 reports the TAC results and discussions of possible potential mechanisms, followed by conclusions in Section 5. In Appendix A, sensitivity experiments are detailed which determined the suitable number of IPs needed in S_TIDE to extract reliable inter-annual and decadal tidal variability in the SCS.

2. Study domain and data

2.1 Study domain

The SCS (Figure 1(a)) consists of a central deep basin and shallow shelf sea in the

North and Southwest (Green and David, 2013). As the largest marginal semi-closed sea in the Northwest Pacific Ocean, it plays a vital role in water mass exchange between the Indian Ocean and the Pacific Ocean (Gao et al., 2015). Previous studies have discussed the motion of the tidal waves and the tidal energy balance in the SCS using numerical models and tide gauge observations (Fang et al., 1999; Zu et al., 2008). Although the K_1 and O_1 tides are much smaller than M_2 tide at the Luzon Strait, which is the major connection of the SCS and the greater Pacific,, they are dominant constituents in the most parts of the SCS (Fang et al., 1999). The largest amplitudes of K_1 (exceeding 80 cm) and O_1 (exceeding 90 cm) appear in the Gulf of Tonkin. In the central deep basin of the SCS, tidal currents are relatively weak (generally less than 2cm/s). Due to the influence of complicated bathymetry, monsoons, and Kuroshio intrusions, the SCS has one of the world's most dynamic ocean environments (Wang et al., 2019). Therefore, the SCS is a hotspot for the research of oceanic internal waves, typhoons, western boundary currents and mesoscale eddies (Wang et al., 2019). A significant number of studies have investigated the generation and propagation of internal tides in the SCS which can cause strong tidal energy dissipation (Jan et al., 2007, 2008; Alford, 2008; Alford et al., 2011; Simmons et al., 2011; Xie et al., 2008, 2011, 2013). However, to date, no studies have investigated the long-term tidal changes in the central deep basin of the SCS because of the shortage of long-term high-frequency sea level observations.

2.2 Water Level Observations

The satellite altimeter data is downloaded from the Radar Altimeter Database System (RADS, http://rads.tudelft.nl/rads/rads.shtml) over a 25-year period (from October 1992 to September 2017), including T/P altimeter data (1992/10-2005/06), Jason-1 data (2002/03-2012/03), Jason-2 data (2008/09-2017/05) and Jason-3 data (2016/04-2017/09). These satellites share the same orbit with a sampling period of 9.9156 days. Compared to other altimeter satellites, T/P-Jason satellite observations have shorter sampling period and longer length of records (LOR). Thus, T/P-Jason altimeter data are widely used in the research of tidal dynamics. Figure 1(b) (red lines) displays the ground tracks of T/P-Jason satellite altimetry in the SCS. To ensure the reliability of the results, we only use 1600 points in Figure 1 (black lines) which are selected based on the LOR (more than 18.61 years) and data completeness (more than 80%).

Hourly water level records from 24 tide gauges in the SCS (Figure 1(b)) are downloaded from the University of Hawaii Sea Level Center (https://uhslc.soest.hawaii.edu/). These tide gauges are also selected according to the LOR and data completeness which are same as satellite data; detailed information is shown in Table 1. Most tide gauges used are provided by China and Malaysia. Although water level observations at Xiamen, Shanwei, Zhapo, Beihai, Haikou, Dongfang are outdated (~1976 to 1997 at most locations) compared to other gauges, they are still analyzed considering the scarcity of tide gauges in the SCS. The water level observations span the period of 1954-2019. Of the 24 records available, 16 are longer than 30 years (Table 1). The Haikou tide gauge has the shortest LOR (only 22 years) while Xiamen gauge has the longest LOR (44 years). The Quarry Bay tide gauge was established originally in 1952 at North Point (Devlin et al., 2019b). Until 1986, this tide gauge moved half a kilometer away to Quarry Bay (Feng et al., 2015). Satellite observations are mainly located in the central deep basin of the SCS while tide gauges are all located in the coastal areas.

Table 1 Coastal tide gauges in the South China Sea used in this study. Locations are displayed in Figure 1(b).

Station	Country	UHSLC number	Number in this paper	Latitude (° N)	Longitude (° E)	Time Span
Kelang	Malaysia	140	1	3.05	101.36	1983-2015
Keling	Malaysia	141	2	2.22	102.15	1984-2015
Lumut	Malaysia	143	3	4.24	100.61	1984-2015
Penang	Malaysia	144	4	5.42	100.35	1984-2015
Cendering	Malaysia	320	5	5.27	103.19	1984-2015
Kuantan	Malaysia	322	6	3.98	103.43	1983-2015
Tioman	Malaysia	323	7	2.81	104.14	1985-2015
Sedili	Malaysia	324	8	1.93	104.12	1986-2015
Kukup	Malaysia	325	9	1.33	103.44	1985-2015
Geting	Malaysia	326	10	6.23	102.11	1986-2015
Ko Lak	Thailand	328	11	11.80	99.82	1985-2019
Quarry Bay	China	329	12	22.30	114.22	1986-2019
Kaohsiung	China	340	13	22.62	120.28	1980-2016
Manila	Philippines	370	14	14.59	120.97	1984-2015
Xiamen	China	376	15	24.45	118.07	1954-1997
Kota Kinabalu	Malaysia	386	16	5.98	116.07	1987-2015
Bintulu	Malaysia	387	17	3.22	113.07	1992-2015
Sandakan	Malaysia	389	18	5.81	118.07	1993-2015
Zhapo	China	635	19	21.58	111.83	1975-1997
Beihai	China	636	20	21.48	109.08	1975-1997

Dongfang	China	637	21	19.10	108.62	1975-1997
Haikou	China	638	22	20.02	110.28	1976-1997
Shanwei	China	641	23	22.75	115.35	1975-1997
Tanjong Pagar	Singapore	699	24	1.26	103.85	1984-2016

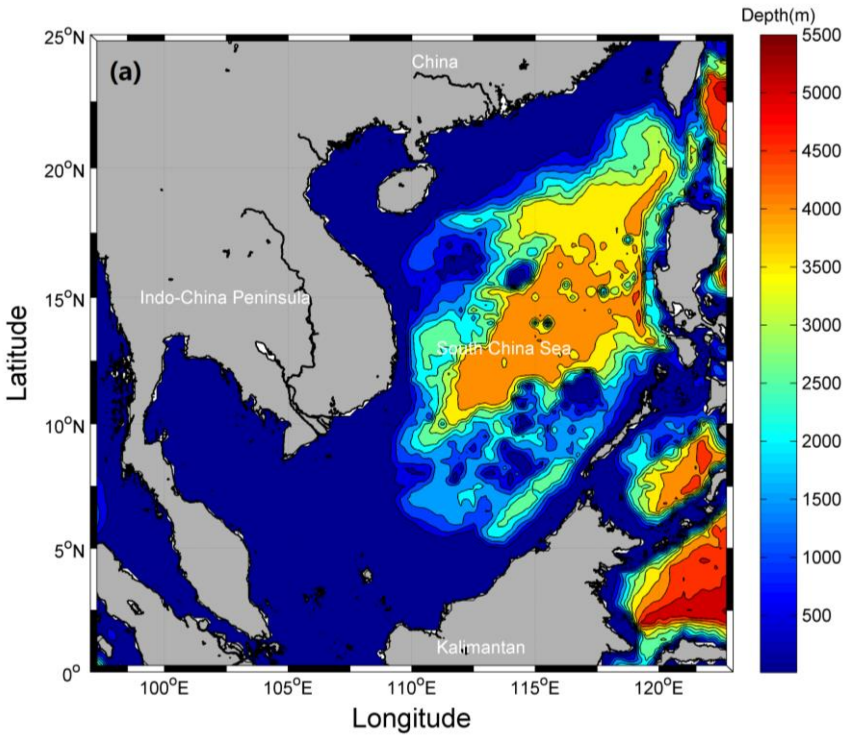

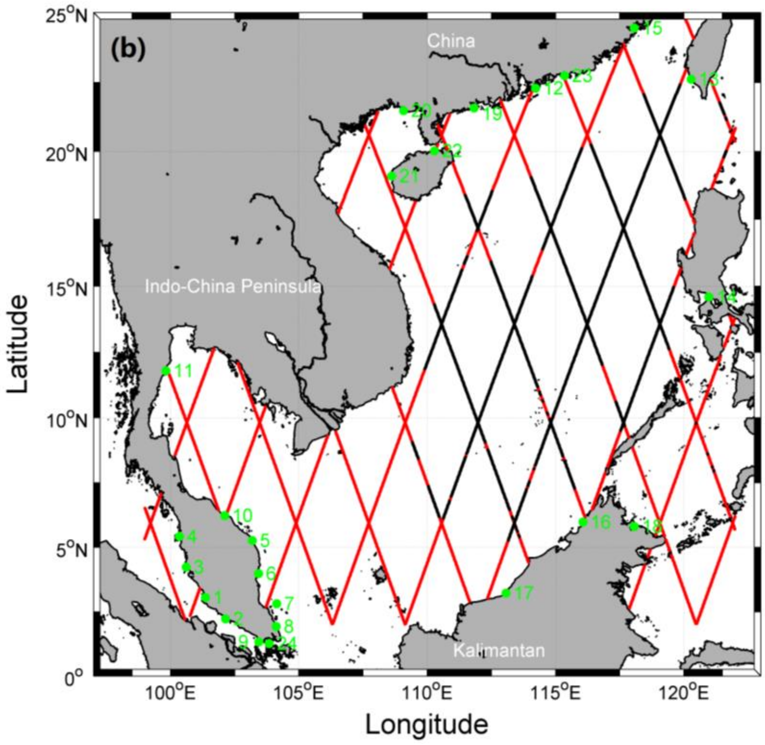

Figure 1. (a) Map of the South China Sea (SCS). (b) Tide gauges and satellite data used in this study. Red lines are the T/P-Jason satellite altimetry tracks in the SCS. Black lines are positions selected for this study. Green dots indicate the tide gauge locations.

3. Methodology

3.1 Enhanced Harmonic Analysis (EHA)

CHA assumes that water levels can be represented by a linear combination of tidal constituents which can be effectively approximated by sinusoidal functions (Foreman and Henry, 1989):

$$H(t) = S_0 + \sum_{i=1}^{I} f_i h_i \cos(w_i t + u_i - g_i) \quad (1)$$

where $H(t)$ is the observed water level at time *t*. w_i, h_i and g_i are the frequency, amplitude and phase corresponding to the *i*-th tidal constituent, respectively. S_0 is the mean water level (MWL). f_i and u_i are nodal factor and angle corresponding to the i-th tidal constituent, respectively. Eq.(1) can be linearized using the new unknows A_i and B_i by rewriting as follows:

$$H(t) = S_0 + \sum_{i=1}^{I} (f_i A_i \cos(w_i t + u_i) + f_i B_i \sin(w_i t + u_i)) \tag{2}$$

where

$$h_i = \sqrt{A_i^2 + B_i^2}, \quad g_i = \arctan(B_i / A_i) \tag{3}$$

Constant A_i and B_i in Eq.(2) can be estimated through ordinary least squares (OLS) regression. Different from CHA, EHA assumes that S_0, A_i and B_i are time-varying, and thus, Eq.(2) is modified as follows:

$$H(t) = S(t) + \sum_{i=1}^{I} (f_i A_i(t) \cos(w_i t + u_i) + f_i B_i(t) \sin(w_i t + u_i)) \tag{4}$$

Eq.(4) is solved through the IP scheme (Pan et al., 2017; Zong et al., 2018). The MWL and tidal coefficients (A and B) at IPs, which are uniformly distributed in the time domain, are selected as independent parameters (denoted as S_j, $a_{i,j}$, and $b_{i,j}$), and those at other points are obtained by interpolation of values at IPs (Pan et al., 2018b). In the IP scheme, $S(t)$, $A_i(t)$ and $B_i(t)$ are expressed by linear combinations of the values at IPs (Eq.(5)). $l_{t,j}$ in Eq.(5) is the known interpolation weight for the j-th IP at time t, which only depends on the interpolation method. N_s and N are the IP numbers for MWL and tidal coefficients, respectively. Note that the values at IPs (namely S_i, $a_{i,j}$, and $b_{i,j}$) are unknown at present, but when using the IP approach, we combine the values at IPs to obtain time varying MWL and tidal coefficients.

$$
\begin{aligned}
S(t) &= \sum_{j=1}^{N_s} l_{t,j} S_j \\
A_i(t) &= \sum_{j=1}^{N} l_{t,j} a_{i,j} \\
B_i(t) &= \sum_{j=1}^{N} l_{t,j} b_{i,j}
\end{aligned}
\tag{5}
$$

Combining Eqs.(4) and (5) yields Eq.(6)

$$
\begin{aligned}
H(t) = {} & \sum_{j=1}^{N_s} l_{t,j} S_j + \\
& \sum_{i=1}^{I} \left(\sum_{j=1}^{N} l_{t,j} a_{i,j} f_i \cos(w_i t + u_i) + \sum_{j=1}^{N} l_{t,j} b_{i,j} f_i \sin(w_i t + u_i) \right)
\end{aligned}
\tag{6}
$$

A cubic spline interpolation is adopted in the IP scheme mainly due to its stability and smoothness (Pan et al., 2017, 2018b). The computation of the cubic spline interpolation weight is described in detail in Appendix B in Pan et al. (2018b), which is not shown here for brevity. There are a total of $2IN+N_s$ unknowns in Eq.(6), which can be estimated via least squares fitting when *M*, the number of observations, is much larger than the number of the unknowns. Finally, $S(t)$, $A_i(t)$ and $B_i(t)$ can be obtained by interpolating S_i, $a_{i,j}$, and $b_{i,j}$ according to Eq.(5).

The selection of the number of IP is critical for S_TIDE. The MWL and tidal amplitudes and phases obtained by S_TIDE using different IP numbers represent oscillations on different time scales (Pan et al., 2018b). More IPs means that more complex changes (or more high-frequency oscillations) of tidal properties can be reproduced, and vice versa. When the IP number is set to 2, S_TIDE can only calculate the linear trend of A_i and B_i as well as MWL. When the IP number is set to 1, S_TIDE can only calculate constant MWL and tidal properties similar to CHA.

There is a trade-off between the number of IP and the constituents included in S_TIDE (Pan et al., 2018b). If we increase the number of IPs, the constituents that S_TIDE can resolve will be fewer. For example, if we want to use S_TIDE to extract the annual variation of M_2 tide, then, the H_1 and H_2 tide (also often denoted as MA_2 and MB_2) cannot be resolved in S_TIDE since H_1 and H_2 derive from annual variation of M_2 tide. Simply put, as the number of IP increases, estimates of the M_2 tide obtained by S_TIDE includes more contributions from its nearby frequencies.

Table 2． Tidal periods and T/P alias periods for ten major tidal constituents

Tidal Constituent	Tidal Period (days)	Alias Period (days)
Sa	365.2422	365.2422
Ssa	182.6211	182.6211
O_1	1.0758	45.7141
K_1	0.9973	173. 1930
M_2	0.5175	62.1074
S_2	0.5000	58.7417
Q_1	1.1195	69.3640
P_1	1.0027	88.8909
N_2	0.5274	49.5283
K_2	0.4986	86.5971

3.2 Processing altimeter data using EHA

In the process of analyzing altimeter data, we must consider the aliasing effect. The periods of the diurnal and semi-diurnal constituents are shorter than twice the T/P repeat period (9.9156 days), thus aliasing is induced according to the Nyquist sampling theorem. Table 2 displays the tidal periods and T/P alias periods of ten major constituents. Note that for the long-period constituents Ssa and Sa, no aliasing is involved. To fully separate two constituents of alias periods T_i and T_j, the LOR must satisfy Eq.(7) based on the Rayleigh criterion:

$$LOR \geq \left| \frac{T_i T_j}{T_j - T_i} \right| \tag{7}$$

As displayed in Table 3 (derived from Eq.(7) and Table 2), full resolution of the M_2 and S_2 tide from T/P-Jason satellite altimeter data requires least 2.97-year observations. To fully separate K_2 from P_1, and K_1 from Ssa, at least 9.18-year records are needed (Table 3). Since the T/P-Jason records used here are longer than 18.61 years, ten major constituents, namely, M_2, S_2, K_1, O_1, P_1, N_2, K_2, Q_1, Ssa and Sa can be resolved in the harmonic analysis. In the harmonic model (Eq.(4)), we use theoretical values of nodal factors and angles to correct the 18.61-year nodal cycles in tides. It is assumed that the actual nodal modulations of tides in the deep sea should be consistent with equilibrium theory.

Because K_2 and P_1 are too close in terms of alias periods, it is impossible for S_TIDE to extract their inter-annual variability. Thus, for K_2 and P_1, as well as K_1 and Ssa tide, we only set two IPs for them which can only obtain their linear trends. S_2 is not so close in frequency to M_2, so it is possible for S_TIDE to extract inter-annual tidal variability of them simultaneously. As indicated in section 3.1, both the M_2 and S_2 tide estimates obtained by S_TIDE will absorb energy from their nearby frequencies if more than one IP is used. As the number of IP increases, estimates of the M_2 and S_2 tide obtained by S_TIDE will be contaminated by nearby frequencies. When the number of IP increases to a critical value, the overlap in the bandwidths of M_2 and S_2 will yield an incorrect estimation of M_2 and S_2 amplitudes. To avoid this situation and also considering that M_2 is more important than S_2, we use only 2 IPs for the S_2 tide. The selection of IP numbers for O_1 and N_2 follows a similar logic. Finally, for the M_2 and O_1 tide, we can use enough IPs to extract inter-annual and decadal variability, while for other constituents only 2 IPs are used to allow trend extraction. In Appendix A, we discuss how many IPs are suitable for extracting inter-annual and decadal tidal variability in the SCS through sensitivity experiments. It is found that for the M_2 and O_1 constituents, about 17 IPs are optimal.

It should be noted that the SCS is known to exhibit significant mesoscale eddy activity (Zhang et al. 2013). The presence of such strong mesoscale activity can influence the accuracy of tidal estimation from altimetry time series (Ray and Zaron, 2016). Ray and Byrne (2010) used multi-satellite mapped sea level anomaly (SLA) fields as a prior correction for the mesoscale ocean variability before tidal harmonic analysis and found that this method can significantly improve the along track altimeter tidal estimates. Zaron and Ray (2018) found that there were residual tidal signals in the mapped SLA fields and implemented several low-pass and bandpass filters to remove residual tidal signals. To ensure the M_2 and O_1 amplitudes obtained using S_TIDE are purely tidal, we use the filtered version of the daily gridded multi-satellite SLA products (including ERS-1/2, ENVISAT, Geosat Follow-on, Cryosat-2, AltiKa, Haiyang-2A, and T/P-Jason satellites) as a prior correction. The readers are referred to Zaron and Ray (2018) for a detailed description of this SLA product. As shown in Figure 2, the correction for mesoscale variability significantly decreases the errors of tidal amplitudes and eliminates false oscillations in tidal amplitudes.

Table 3. Minimum length (years) for resolving each pair of constituents in T/P, Jason1, and Jason2 satellites (Ray 1998)

	S_{sa}	Q_1	O_1	P_1	K_1	N_2	M_2	S_2	K_2
S_a	1.00	0.23	0.14	0.32	0.90	0.16	0.20	0.19	0.31
S_{sa}		0.31	0.17	0.47	**9.18**	0.19	0.26	0.24	0.45
Q_1			0.37	0.86	0.32	0.47	1.63	1.05	0.95
O_1				0.26	0.17	1.63	0.47	0.56	0.27
P_1					0.50	0.31	0.56	0.47	**9.18**
K_1						0.19	0.27	0.24	0.47
N_2							0.67	0.86	0.32
M_2								2.97	0.60
S_2									0.50

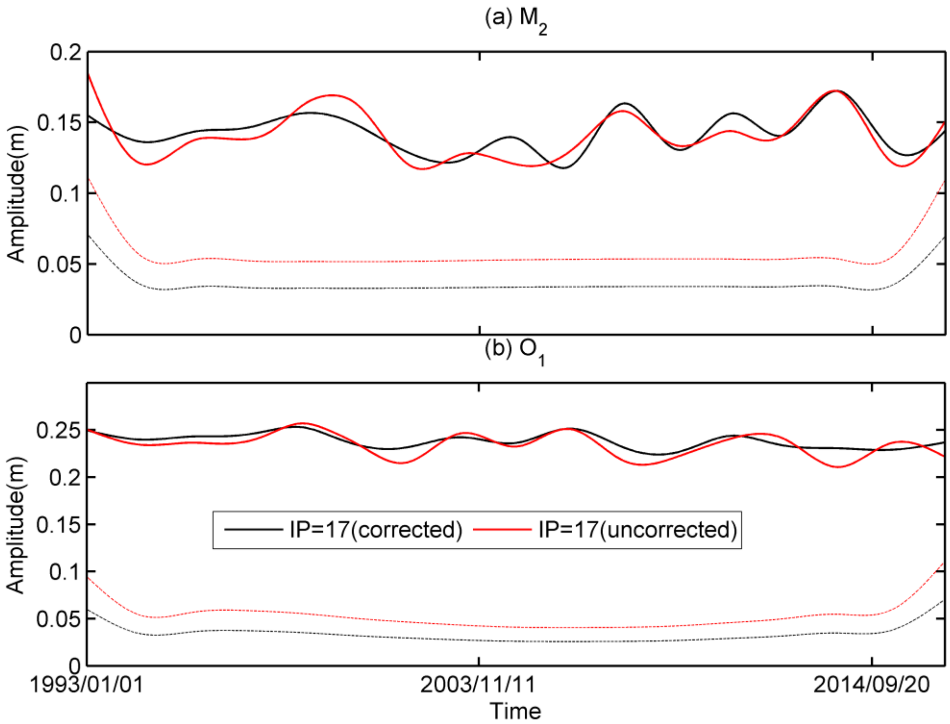

Figure 2 (a) M_2 tidal amplitudes (solid lines) and their errors (dash lines) obtained by S_TIDE with 17 IPs at 15.33° N, 118.38° E. Black lines are derived from sea level observations corrected for mesoscale variability. (b) Same as (a), but for O_1 amplitudes.

3.3 Processing tide gauge data using CHA

For hourly tide gauge observations, yearly (8767 hours) classical harmonic analysis windows are employed, using the T_TIDE MATLAB toolbox (Pawlowicz et al., 2002) at monthly (720 hours) time steps. Yearly windows are used to filter annual and sub-annual tidal variability and are long enough for resolving P_1 (K_2) from K_1 (S_2). 67 tidal constituents (including 6 long-period constituents and 22 shallow water constituents) can be resolved according to LOR and Rayleigh criterion. MWL time series are also generated in the course of CHA. Note that theoretical nodal corrections are not applied in the course of CHA because the actual nodal modulations of tidal amplitudes and phases have been often observed to be different from equilibrium theory in many coastal regions around the world (Amin, 1985,1993; Woodworth et al., 1991; Ray 2006; Feng et al., 2015; Pan et al., 2019). For instance, at the Portland tide gauge, USA, located in the Gulf of Maine, the 18.61-year nodal modulation of M_2 amplitude is sharply reduced from 3.73% to 2.77% due to the effects of resonance and nonlinear bottom friction (Ku et al., 1985; Ray 2006; Ray and Talke, 2019).

We remove 18.61-year nodal cycles in main constituents using a widely used regression model (Ku et al., 1985; Ray 2006, 2009; Jay 2009; Feng et al., 2015) which is expressed as:

$$A(t) = C_0 + C_1 t + H_N \cos\left(\frac{2\pi}{18.61} t + G_N\right) \quad (8)$$

where $A(t)$ are the estimated values of tidal amplitudes or phases at time t. C_0 is a constant, C_1 is the linear trend. H_N and G_N are the amplitude and phase of the nodal cycle, respectively. Instead of ordinary least squares, robust fitting (Leffler and Jay, 2009) which can significantly reduce the contribution of high-leverage data points is used to estimate the model parameters.

Table 4 displays the actual nodal modulation of the tidal amplitudes of four major tides in the SCS. At most tide gauges, actual nodal cycles are distinct from theoretical values. The actual nodal modulations of M_2 amplitudes vary from 2.5±0.1% (Xiamen) to 11.1±0.2% (Haikou) while those of S_2 range from 0.0±0.1% (Penang) to 4.4±0.4% (Beihai). The actual modulations of K_1 amplitudes vary from 7.9±0.3% (Bintulu) to 12.9±0.2% (Sedili) while those of O_1 range from 11.3±1.3% (Kelang) to 25.8±1.2%

(Lumut). Figure 3 shows the actual nodal modulations of the M_2 and O_1 tidal amplitudes at Quarry Bay, Hong Kong as an example. The exact reversed variations of M_2 and O_1 nodal cycles indicate that the M_2 and O_1 nodal phases are generally consistent with theory. The M_2 (O_1) nodal amplitude is 32.1±1.2 (45.1±1.3) mm while the mean M_2 (O_1) tidal amplitude is 389.0 (293.3) mm. The Quarry Bay gauge is located in Victoria Harbour which is seriously influenced by human activities such as harbor construction and land reclamation (Devlin et al., 2019b). Such anthropogenic intervention may be responsible for the deviations from the equilibrium theory. Another possible factor that may affect nodal variability involves resonant triads, which are nonlinear interactions between the M_2 and K_1/O_1 tides which may transfer energy to each other, and in cases may decrease the K_1/O_1 nodal modulations and increase the M_2 nodal modulation. This type of behavior has been confirmed in the Solomon Sea (Devlin et al., 2014), and is suggested from observations at tide gauges in the southern part of the Gulf of Thailand. Similarly, strong nodal modulations in the S_2 tide is not expected to be affected by the lunar nodal cycle and instead may be related to nonlinear interactions between the M_2 and S_2 tides (Feng et al., 2015). The possible causes of discrepancies between observed and theoretical nodal cycles at other tide gauges are not discussed because this is not the main focus of this paper.

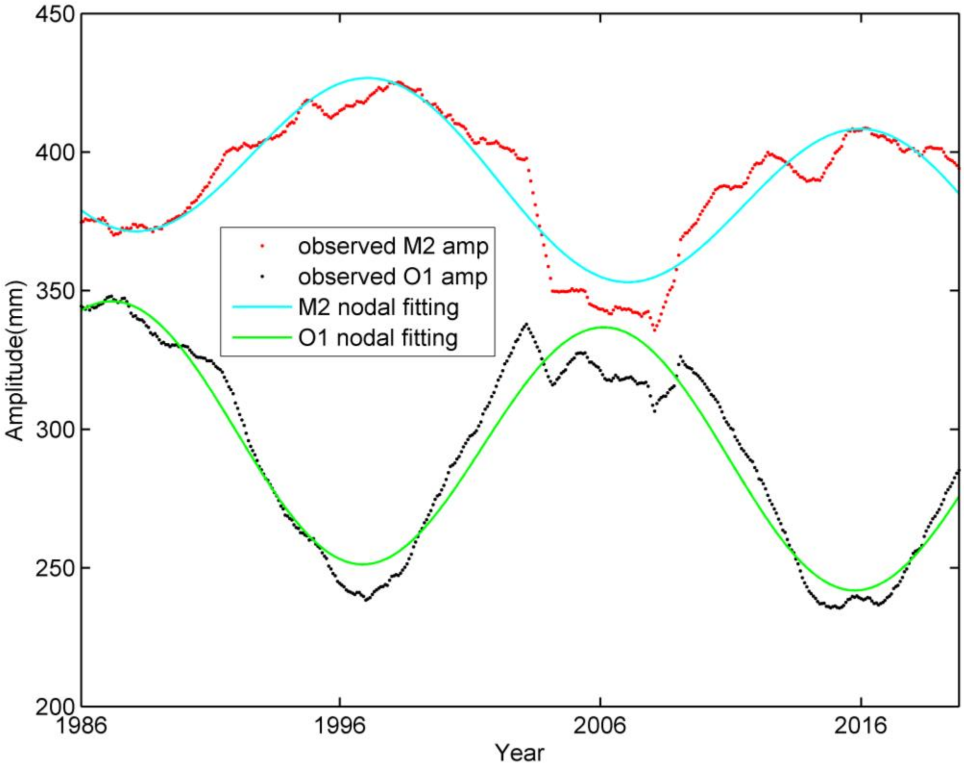

Figure 3 M_2 /O_1 tidal amplitudes (red/black dots) and their nodal fitting results (cyan/green lines) at Quarry Bay, Hong Kong.

Table 4 18.61-year nodal modulations of tidal amplitudes of main constituents in the South China Sea. Note that statistically insignificant values are given in italic text.

Constituents	M_2	S_2	K_1	O_1
Theoretical	3.73	0	11.5	18.7
Kelang	3.7±0.1	0.7±0.1	12.6±0.3	11.3±1.3
Keling	3.4±0.1	2.0±0.1	11.9±0.7	14.5±0.2
Lumut	3.7±0.1	0.6±0.1	11.8±0.2	25.8±1.2
Penang	4.1±0.1	*0.0±0.1*	11.5±0.2	21.3±0.6
Cendering	4.6±0.1	0.7±0.2	10.9±0.1	19.2±0.2
Kuantan	5.6±0.1	1.3±0.2	11.5±0.1	19.4±0.1
Tioman	5.5±0.1	1.3±0.1	12.1±0.1	19.8±0.1
Sedili	5.3±0.1	1.0±0.1	12.9±0.2	19.9±0.2
Kukup	3.2±0.1	1.9±0.1	10.2±0.2	16.6±0.2
Geting	3.1±0.5	2.5±0.5	11.8±0.2	18.7±0.2
Ko Lak	5.6±0.5	*1.8±1.9*	10.0±0.2	18.1±0.3
Quarry Bay	8.3±0.3	3.4±0.3	8.0±0.4	15.4±0.5
Kaohsiung	3.6±0.3	*0.4±0.4*	10.9±0.2	18.2±0.3
Manila	3.7±0.7	*0.4±0.6*	12.8±0.4	19.3±0.5
Xiamen	2.5±0.1	1.8±0.1	10.8±0.1	18.3±0.2
Kota Kinabalu	3.9±0.1	0.2±0.1	10.6±0.1	18.3±0.1
Bintulu	4.6±0.3	1.4±0.3	7.9±0.3	14.0±0.6
Sandakan	3.8±0.4	0.7±0.1	10.8±0.2	17.2±0.4
Zhapo	4.3±0.1	*0.1±0.2*	11.1±0.1	18.3±0.2
Beihai	10.4±0.2	4.4±0.4	8.2±0.1	16.0±0.2
Dongfang	8.5±0.1	1.4±0.2	8.0±0.1	15.9±0.2
Haikou	11.1±0.2	1.3±0.2	9.9±0.1	17.2±0.2
Shanwei	5.4±0.1	1.8±0.2	11.1±0.1	18.3±0.2
Tanjong Pagar	3.9±0.8	0.5±0.1	12.1±0.2	18.4±0.2

3.4 Tidal Anomaly Correlation (TAC) method

The TAC method proposed by Devlin et al. (2017a) has been used to analyze co-variability of tidal amplitudes and MWL in the Pacific Ocean (Devlin et al., 2017a), Atlantic Ocean (Devlin et al., 2019a) and Hong Kong region (Devlin et al., 2019b). By the combination of the ensemble empirical mode decomposition (EEMD) and

TAC method, Devlin et al. (2020) analyzed multi-timescale tidal variability (semi-annual, annual, and multi-year) in the Indian Ocean. As shown in Eq.(9), the slope *k* of the linear regression between detrended tidal amplitudes *H(t)* and detrended MWL *S(t)* is the definition of the TAC.

$$H(t) = k * S(t) + b \tag{9}$$

The mean and trend in these time series must be removed before regression because the trends may be influenced by tidal and sea level variability on longer time scale while here we are interested in non-astronomical inter-annual and decadal variability. The TACs and their errors are estimated by robust fitting and expressed in units of mm/m. To ensure the regression is valid and the obtained TAC is significant, we require that the signal-to-noise ratio (SNR) should be larger than 2.0. We only focus the TACs of four major tidal constituents, M_2, S_2, K_1 and O_1 in this research. In the original TAC method, tidal amplitudes are divided by astronomical tidal potential (namely tidal admittance technique) to remove the long-period astronomical variability like the 18.61-year nodal cycles. However, as mentioned above, nodal cycles in tidal amplitudes may not be completely removed using the tidal admittance technique due to the discrepancies between observed and theoretical nodal modulations. The residual nodal cycle in tidal amplitudes may significantly influence the estimation of TACs as well as their errors at some tide gauges. Therefore, instead of the tidal admittance technique, we use Eq.(8) to remove the nodal cycles.

Figure 4 displays the K_1 and O_1 TAC results at Sandakan tide gauge (5.81° N, 118.07° E) which are two of the clearest signals in the SCS. Both K_1 and O_1 TAC are quite large and coherent, 68.9 ± 6.9 mm/m and 101.4 ± 14.7 mm/m, respectively. In other words, the K_1 and O_1 amplitudes increase 68.9 mm and 101.4 mm per meter sea level change, respectively. As shown in Figure 4(b), the red dots in the blue box are outliers and their effect on the estimation of the TAC is eliminated by the application of robust linear regression. If we use tidal amplitudes preprocessed by the tidal admittance technique, the estimated K_1 and O_1 TAC results at Sandakan are 43.7±19.3 mm/m and 47.4 ± 36.9 mm/m, respectively. The residual nodal cycles therefore significantly decrease the TAC values, and also increase the errors of TACs. The O_1 TAC actually becomes statistically insignificant at Sandakan due to the residual nodal cycle.

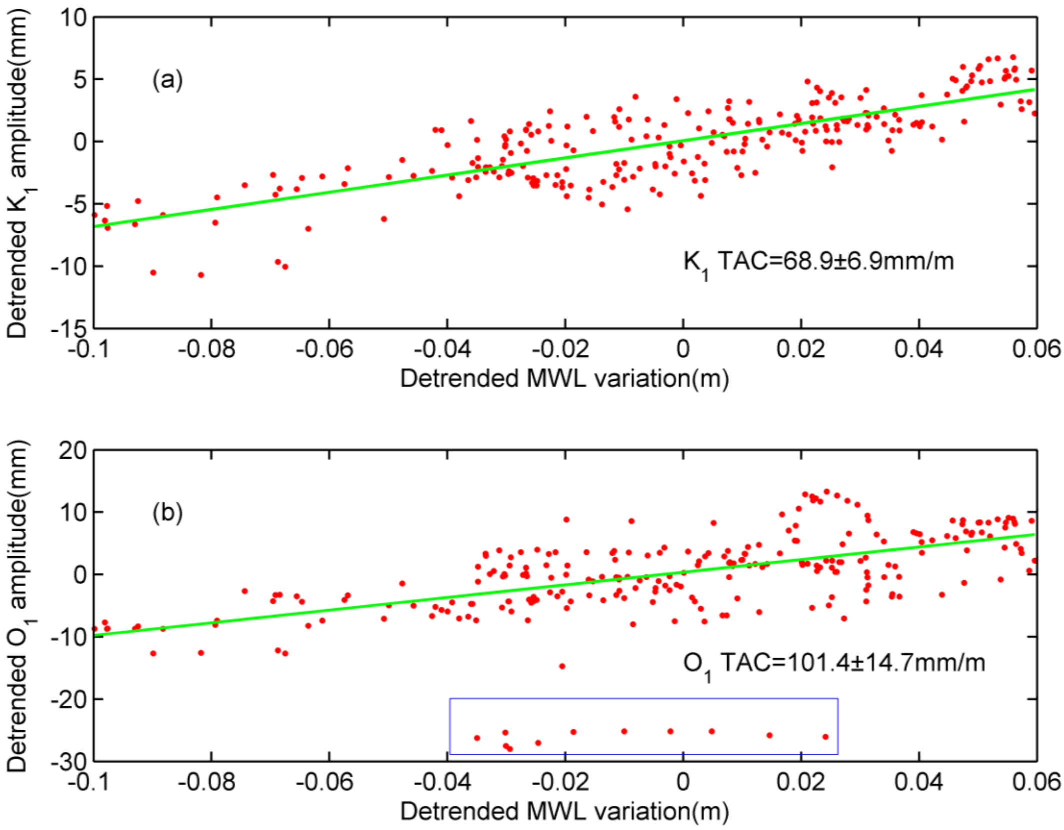

Figure 4 Example regression of the tidal anomaly correlation (TAC) method at Sandakan tide gauge (5.81° N, 118.07° E). (a) K_1 TAC relation of detrended tidal amplitudes to detrended MWL. (b) Same as (a), but for O_1 TAC. In both plots, the red dots are data, the green lines represent the regression. The red dots in the blue box are outliers. Note that nodal cycles in K_1 and O_1 amplitudes are removed by Eq.(8).

4. Results and Discussions

4.1 Tidal Anomaly Correlation (TAC) Results in the Coastal Areas

Figures 6(a) and 6(b) show maps of the TACs for M_2 and O_1 tides in the SCS, respectively. The color bar indicates the magnitude of the TACs. Numeric values of the TACs for the four major tides in the SCS are reported in Table 5. Statistically significant TACs (SNR larger than 2.0) are listed in bold text. For the semidiurnal constituents, M_2 TACs are significant at 19 gauges and range from -141.5 ± 13.3mm/m (Kelang) to 47.3 ± 23.4mm/m (Quarry Bay). S_2 TACs are significant at 17 gauges and range from -49.5 ± 8.0mm/m (Kelang) to 41.0 ± 12.4mm/m (Xiamen). For the diurnal constituents, K_1 TACs are significant at 16 gauges and vary from -81.5 ± 9.7mm/m (Keling) to 97.5 ± 18.5mm/m (Manila). O_1 TACs are significant at 21 gauges and range from -124.1 ± 44.6mm/m (Haikou) to 126.8 ± 37.1mm/m (Bintulu).

The M_2/S_2/K_1/O_1 TACs reveal no basin-scale patterns but do show some regions of locally coherent behavior. At most gauges in the SCS, the M_2 and S_2 TACs are negative while the O_1 TACs are positive. For K_1, the TACs are slightly more often positive than negative. As displayed in Figure 6 and Table 5, at nearly all gauges in Singapore and peninsular Malaysia, the M_2/S_2 TACs are negative except at Tanjong Pagar (S_2 9.1 ± 5.9mm/m) while O_1 TACs are positive everywhere except at Lumut (-10.5 ± 6.6mm/m). There are a few exceptions to these generalizations, though the TACs of these exceptions are relatively small. It should be noted that the SCS has an exceptionally long coastline, thus, only 24 tide gauges are insufficient to represent the overall characters of coastal tidal variability and it is difficult to obtain basin-scale tidal variability without the assistance of other kinds of sea level observations. It is also worth mentioning that Quarry Bay is the only gauge in the SCS whose TACs of all four major constituents are all statistically significant and positive; this may be due to local anthropogenic effects important at this location such as harbor modification and channel deepening (Devlin et al., 2019b). Yet overall，the TAC results indicate that inter-annual and decadal sea level variability is highly correlated to corresponding tidal variability at nearly all tide gauges in the SCS.

Table 5 The tidal anomaly correlations (TACs) (unit: mm/m) of main constituents in the South China Sea. Statistically significant values are given in bold text.

Station	M_2	S_2	K_1	O_1
Kelang	**-141.5±13.3**	**-49.5±8.0**	**23.4±9.3**	**40.4±7.5**
Keling	**-70.8±9.6**	**-34.9±5.1**	**-81.5±9.7**	**37.4±6.4**
Lumut	**-61.5±6.5**	**-33.1±4.1**	**13.5±9.0**	**-10.5±6.6**
Penang	**-85.0±8.7**	**-43.5±4.8**	6.2±5.8	0.6±5.3
Cendering	**-81.0±10.3**	**-27.2±5.6**	-1.1±20.3	**22.3±15.0**
Kuantan	**-99.6±16.9**	**-35.2±8.8**	**-39.9±21.1**	**59.6±15.2**
Tioman	**-104.4±22.2**	**-26.8±7.9**	-27.9±20.9	**57.0±15.4**
Sedili	**-70.0±17.1**	-7.9±8.6	**-39.6±20.6**	**58.6±14.8**
Kukup	**-71.6±11.5**	**-30.1±6.5**	**-28.9±11.1**	**68.2±9.7**
Geting	**-34.0±14.5**	1.0±7.3	**24.1±16.5**	**12.0±7.2**
Ko Lak	**19.1±4.0**	-0.1±2.4	-8.3±14.0	**36.9±14.9**
Quarry Bay	**47.3±23.4**	**28.4±8.8**	**83.5±30.7**	**58.4±27.5**
Kaohsiung	**40.3±14.1**	-2.6±8.2	**18.3±11.3**	**34.1±13.3**
Manila	**-42.8±8.2**	**-20.3±3.8**	**97.5±18.5**	**-27.3±9.1**
Xiamen	**45.8±23.3**	**41.0±12.4**	**-14.3±9.3**	-1.4±12.4
Kota Kinabalu	**-27.3±3.5**	**-7.9±1.6**	-7.9±8.8	**19.0±10.7**
Bintulu	-15.0±10.9	-1.1±3.8	**69.3±25.6**	**126.8±37.1**
Sandakan	**19.1±8.2**	**-11.1±5.4**	**68.9±6.9**	**101.4±14.7**
Zhapo	**-54.2±17.9**	3.4±15.2	-15.4±16.8	**-84.4±21.2**
Beihai	-9.9±22.5	**26.4±14.1**	**61.4±31.3**	23.4±77.3
Dongfang	-8.1±8.4	**9.2±3.7**	-0.6±20.6	**-114.0±52.1**
Haikou	-26.0±18.4	-3.4±10.7	**-45.1±18.3**	**-124.1±44.6**
Shanwei	**-13.2±8.9**	**-13.1±6.0**	13.9±17.4	**-43.6±25.3**
Tanjong Pagar	-8.6±11.8	**9.1±5.9**	**-33.4±11.7**	**23.3±10.0**

4.2 Tidal variability in the Deep Water of the South China Sea

4.2.1 TAC Results in the Deep Water of the South China Sea

In this section, we use S_TIDE with 17 IPs to extract the inter-annual and decadal variations of the M_2 and O_1 amplitudes in the central deep basin of the SCS. For the other constituents, two IPs are used. Inter-annual and decadal sea level variations are obtained by filtering the daily gridded multi-satellite SLA fields. For the M_2 (O_1) TACs, there are only 28.3% (26.3%) of total positions (1600) whose SNRs are less than 2.0. Therefore, at most positions in the central deep basin of the SCS, tidal variability and sea level variability are correlated. The M_2 TACs range from -514.9 ± 53.5mm/m to 569.7 ± 62.6mm/m and the O_1 TACs range from -475.6 ± 39.6 to 392.8 ± 29.2 mm/m. Figure 7(a) displays the inter-annual and decadal variations of MWL and M_2 amplitudes (with the trend and mean value removed) at 17.49°N 114.94°E as an example. The correlation coefficient between detrended MWL and detrended M_2 amplitude in Figure 7(a) is -0.85 and the corresponding TAC is -366.1 ± 16.7mm/m. The largest positive M_2 TAC occurs in the Luzon Strait (21.22°N, 121.64°E). At this position, inter-annual and decadal variations of MWL and M_2 amplitudes are positively correlated in most of the time (Figure 7(c)).

The number of positions where tidal variability and sea level variability are positively correlated is slightly smaller than the number of positions where tidal variability and sea level variability are negatively correlated. As shown in Figure 5 and Figure 6, at 37.5% (38.2%) of total positions, the M_2 (O_1) TACs are negative while at 34.3% (35.5%) of total positions, the M_2 (O_1) TACs are positive. However, it should be noted that at most positions, the absolute TACs are less than 200 mm/m. Only at 8.4% (6.8%) of total positions, the absolute values of M_2 (O_1) amplitudes and

MWL correlation coefficients are larger than 200 mm/m indicating that tidal variability has a large response to sea level variability at these locations. The averaged positive M_2 (O_1) TACs are 104.4 (101.1) mm/m while the averaged negative M_2 (O_1) TACs are -125.2 (-110.2) mm/m. The response of M_2 and O_1 tidal amplitudes due to correlated sea level changes (TACs) displays a general mixed pattern of negative and positive responses in the central deep basin of the SCS. There are no coherent basin-scale patterns apparent in the M_2/O_1 TAC results from T/P-Jason data. Some possible mechanisms for such tidal variability in the SCS will be discussed in section 4.3. It seems that there are many areas where adjacent points alternative between negative and positive (Figure 6). This is an optical illusion caused by too many points plotted in small regions. The readers are referred to Figure B1 in Appendix B for a zoomed-in version of Figure 6 which better demonstrates this.

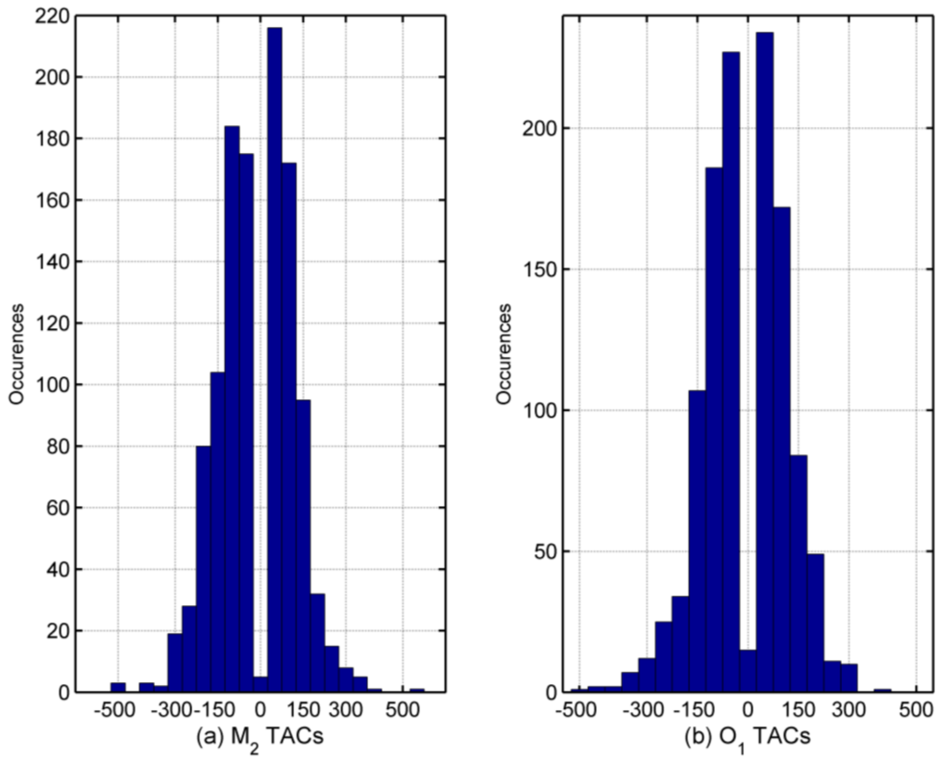

Figure 5. (a) Histogram of M_2 tidal anomaly correlations (TACs) in the central deep basin of the South China Sea (b) same as (a), but for O_1 TACs.

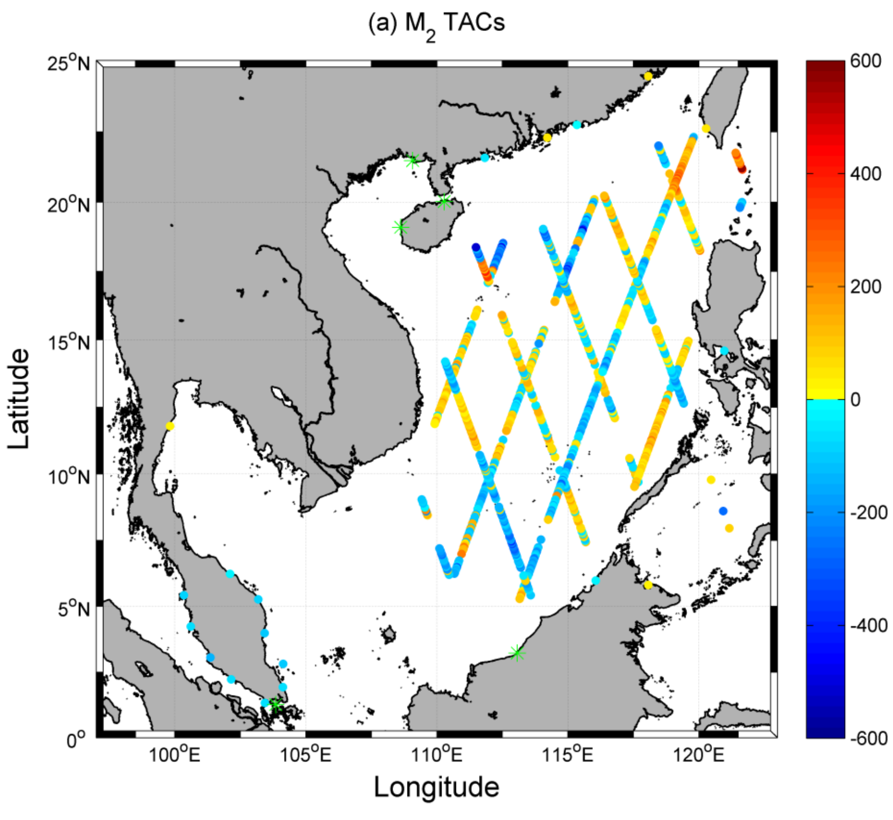

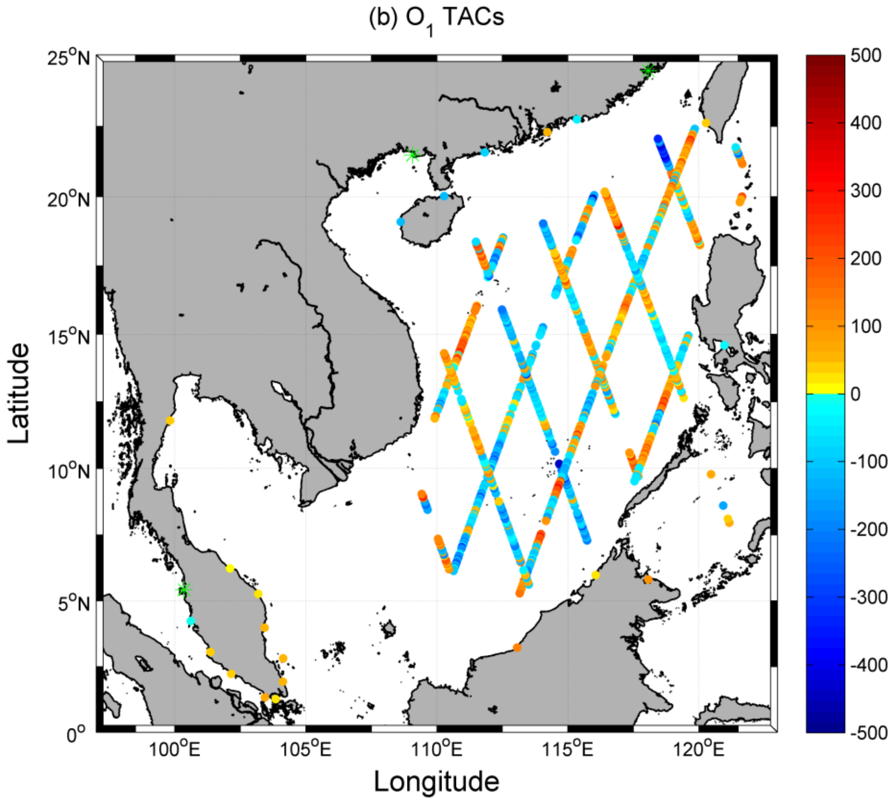

Figure 6 (a) M_2 tidal anomaly correlations (TACs) in the South China Sea (both tide gauges and satellite data are plotted) (b) same as (a), but for O_1 TACs. For satellite data, insignificant TACs are not plotted. For tide gauges, insignificant TACs are labeled as green asterisks.

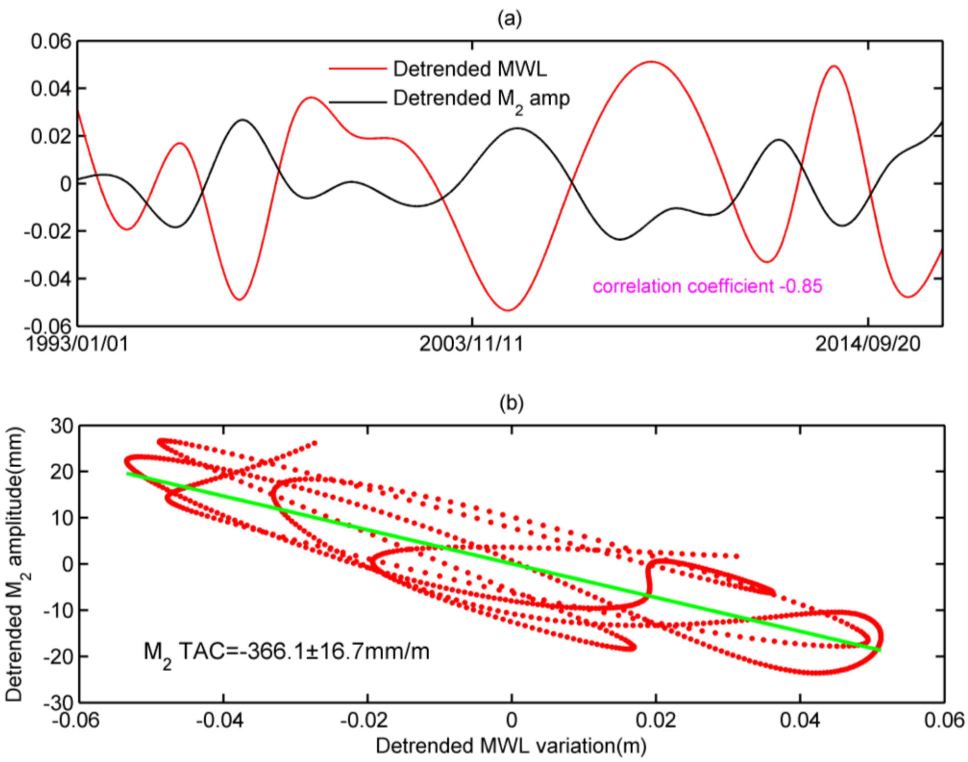

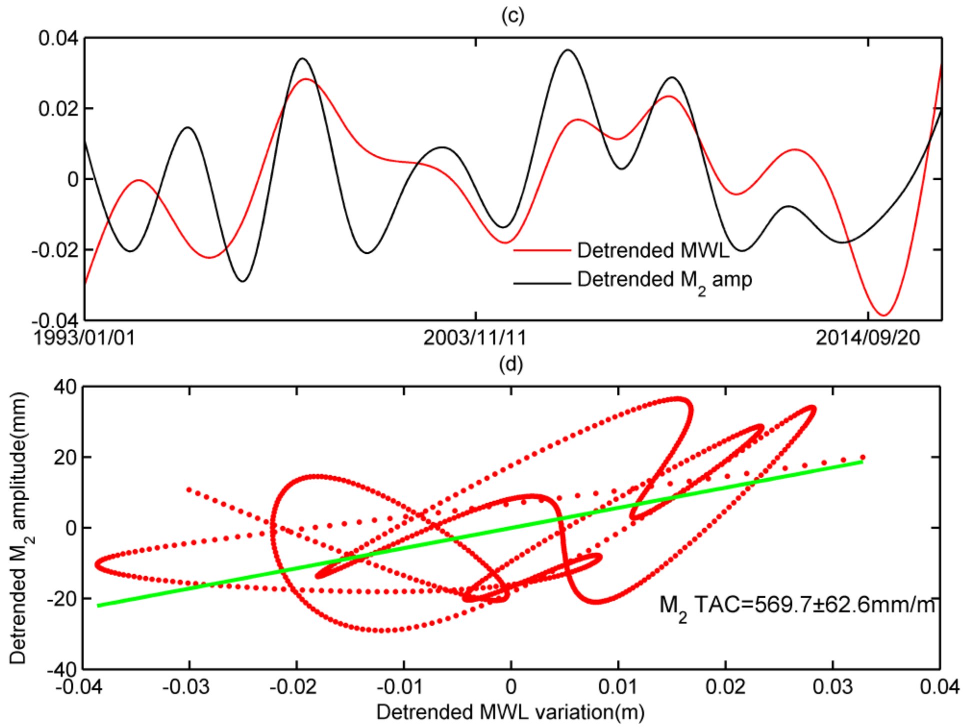

Figure 7 (a) Detrended MWL and M_2 amplitudes (unit: m) obtained by S_TIDE using 17 IPs at 17.49° N, 114.94° E. (b) The M_2 tidal anomaly correlation (TAC) at 17.49° N, 114.94° E (M_2 is in units of mm). (c) Same as (a), but at 21.22° N,

121.64° E. (d) The M_2 tidal anomaly correlation (TAC) at 21.22° N, 121.64° E. The red dots are data, the green line represents the robust linear regression.

4.2.2 Linear Trends of tides in the Deep Water Regions of the South China Sea

For the rest of constituents, non-linear trends of tidal amplitudes are extracted by S_TIDE using 2 IPs. To obtain the linear trends of tidal amplitudes, we perform linear fitting on non-linear trends. For the linear trend to be deemed significant, it must have an SNR greater than 2.0. The results of K_1 and S_2 constituents are shown here for example. The K_1 tide appears to be more significant than the S_2 tide in the central basin of the SCS. For the K_1 (S_2) constituent, there are 62.1% (54.0%) of locations where the linear trends of tidal amplitudes are not significant. The linear trends of S_2 amplitudes vary from -0.161 ± 0.034 cm/yr to 0.139 ± 0.031 cm/yr while those of K_1 amplitudes range from -0.153 ± 0.026 cm/yr to 0.130 ± 0.025 cm/yr. As shown in Figure 8 and Figure 9, at 28.4% (8.69%) of locations, the trends of K_1 (S_2) amplitudes are negative while at 9.5% (37.3%) of locations, the trends are positive. The averaged positive linear trends of K_1 (S_2) amplitudes are 0.062 (0.059) cm/yr while the averaged negative linear trends of K_1 (S_2) amplitudes are -0.063 (-0.056) cm/yr. Note that the negative linear trends of S_2 amplitudes are mainly located in the north of the SCS (Figure 9(b)). At only 3.94% (3.75%) of total positions, the absolute values of the linear trends of K_1 (S_2) amplitudes are larger than 0.09cm/yr which indicates that the tidal dynamics at these positions are undergoing rapid changes.

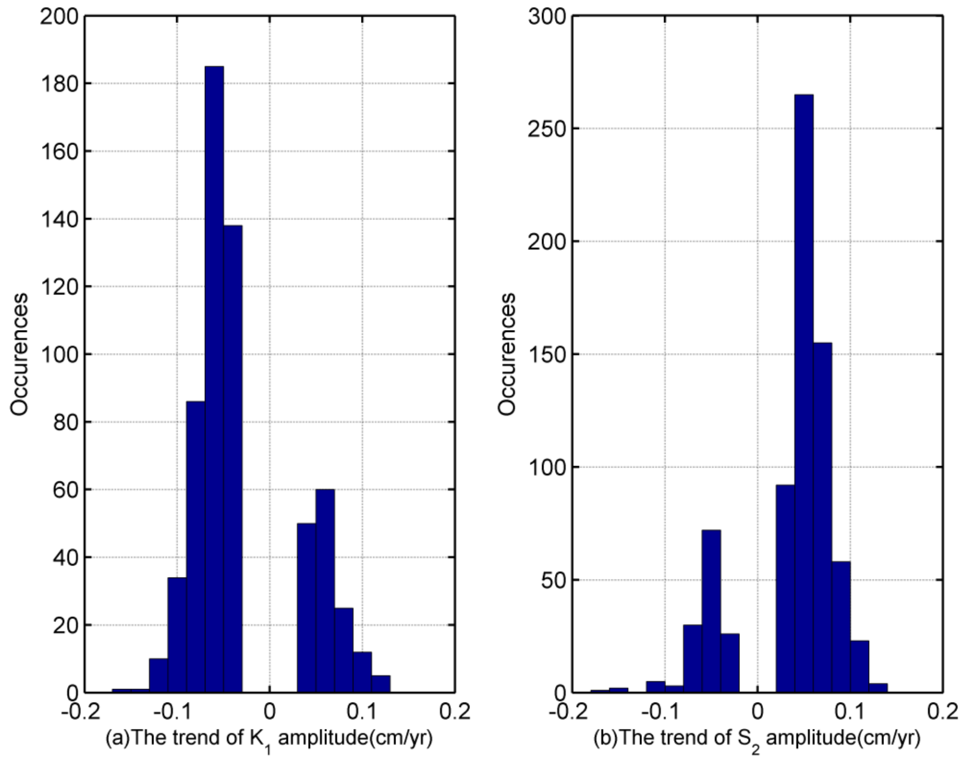

Figure 8 Histogram of linear trends of K_1 and S_2 amplitudes in the central deep basin of the South China Sea. K_1 trends are more often negative, and S_2 trends are more often positive.

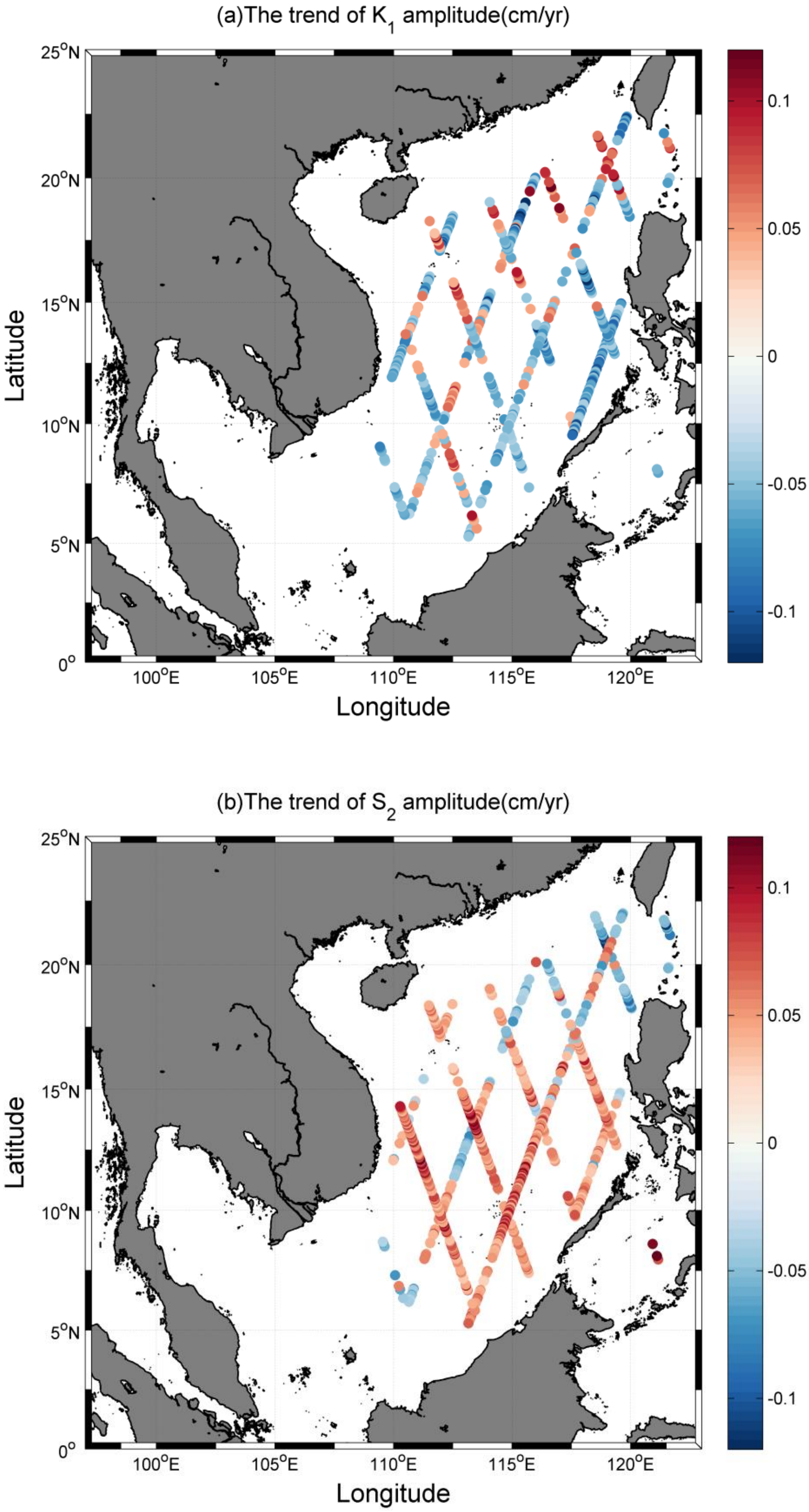

Figure 9. The linear trends of K_1 (a) and S_2 (b) amplitudes in the central deep basin

of the South China Sea. Only significant K_1 and S_2 trends are displayed.

4.3 Discussion

4.3.1 The possible causes for tidal variability in the SCS

Previous studies (Devlin et al., 2017a,b; 2019a,b) have suggested that the variability in tidal amplitudes are nonlinear functions of numerous interrelated variables:

$$\Delta H(t) = f(\Delta h, \Delta Q_r, \Delta\rho, \Delta r, \Delta\psi_w, ...) \quad (10)$$

where h represents the water depth, Q_r is river flow, ρ is water density, r is friction, and ψ_w means frequency-dependent tidal response to astronomical tidal forcing (the subscript w represents tidal frequency). The "Δ" indicates the changes in these variables. The "…" indicates other possible factors not listed here, such as monsoons which may further influence river flow and water density via precipitation (Devlin et al., 2018).

Although the correlations between sea level variability and tidal variability are significant at most positions in the coastal areas and deep sea, the potential mechanisms may be distinct and complex. In coastal areas, the water is very shallow. The variations in sea levels may significantly change the water depth, and thus, alter bottom fiction and influence the propagation of tidal waves (Lu and Zhang, 2006; Devlin et al., 2017a,b, 2019a,b). These shallow-water related mechanisms may be especially important in the Gulf of Thailand, where the average water depth is much smaller than other parts of the SCS. The majority of coastal tide gauges show that tidal variability and sea level variability are closely correlated at inter-annual time scales in the SCS. It should be noted that coastal tides are also significantly influenced by other factors such as river flow and human activities (e.g., channel deepening, harbor construction and land reclamation.). Thus, the sea level variability can only explain part of the tidal variability in the coastal areas.

The T/P-Jason observations studied in this paper are mainly located in the central deep basin of the SCS which are far from the coast (Figure 1(b)). Thus, the tides in this area are likely not strongly influenced by mechanism such as river discharge and human intervention. In the central deep basin of the SCS, the water depth is generally more than 2000m, and the inter-annual and decadal sea level variations are typically much smaller than 1m (see Figure 7 for example) which should not have a significant influence on tides. The tidal variability in this region is possibly related to variations in ocean stratification which is a function of sea water temperature. Another hypothesis is that the inter-annual and decadal variations in sea water temperature may be influenced by climate modes, especially the El Niño–Southern Oscillation (ENSO) (Rong et al., 2007) which may influence tidal variability in this region. Figure 10 and Figure 11 display the correlation coefficients between the M_2 and O_1 amplitudes and the Oceanic Niño Index (ONI) (Figure 12), one of the most commonly used indices to represent oceanic effects of El Niño and La Niña events (https://climatedataguide.ucar.edu/climate-data/). The correlation coefficients between the M_2 amplitude and ONI (considering lags, up to a maximum of 12 months) range from -0.59 to 0.60 while the correlation coefficients between O_1 amplitude and ONI range from -0.65 to 0.57. At 8.1% (8.1%) of total positions, the absolute values of M_2 (O_1) amplitudes and ONI correlation coefficients are larger than 0.4.

The SCS is known for its strong internal tides (Alford, 2008; Alford et al., 2011; Gao et al., 2015), especially in and around the Luzon Strait. The amplitudes of the surface expression of M_2 and K_1 internal tides in the SCS can reach 18 and 20 mm, respectively (Zaron 2019). The generation, propagation, and dissipation of internal tides as well as their surface expression are sensitive to the changes in ocean stratification (Colosi and Munk, 2006; Zhao 2016; Zhai et al., 2020). Therefore, the barotropic tides in the SCS may be modulated by inter-annual and decadal sea water temperature variations via baroclinic energy conversion (Jan et al., 2007, 2008). Note that the surface expression of internal tides which constitutes an important component of total recorded surface tides is also modulated by the changes in sea water temperature (Ray and Mitchum, 1997; Mitchum and Chiswell, 2000; Colosi and Munk, 2006; Devlin et al., 2014). Figure 13 displays the positions (labeled by pink asterisks) where absolute M_2 and O_1 TACs exceed 300mm/m. Nearly all pink asterisks are located in the edge of the central deep basin where water depth changes dramatically in space. These areas including continental slopes and the Luzon Strait have strong baroclinic generation (Jan et al., 2007, 2008).

Numerous studies have indicated that inter-annual sea level variations in the SCS are closely related to ENSO (e.g., Rong et al., 2007; Mohan et al., 2015; Mohan and Vethamony, 2018). The correlation coefficient between the inter-annual components of the mean sea level anomalies and the Southern Oscillation Index (SOI) can reach 0.78 with SOI leading the sea level anomalies by about four months (Rong et al., 2007). The sea level anomalies in the SCS are usually negative during El Ninos, and positive during La Ninas (Rong et al., 2007). Surface wind anomalies associated with ENSO are the most likely explanation for the sea level anomalies in the central deep basin of the SCS (Cheng et al., 2015). Since both inter-annual sea level variability and tidal variability are significantly influenced by ENSO, they are highly correlated at many positions in the central deep basin of the SCS although the direct influence of sea level variability on tidal variability may be negligible.

The long-term linear trends of K_1 and S_2 amplitudes may be related to increasing ocean stratification caused by ocean warming (Colosi and Munk, 2006). Global ocean stratification has increased by 5.3% from 1960 to 2018 (Li et al., 2020). Also, it should be noted that while the K_1 tide is purely gravitational, the S_2 tide is partly influenced by solar-induced radiational forcing (e.g., wind stress, barometric pressure) (Feng et al., 2015). The long-term trends of radiational forcing may also contribute to the long-term trends of S_2 amplitudes.

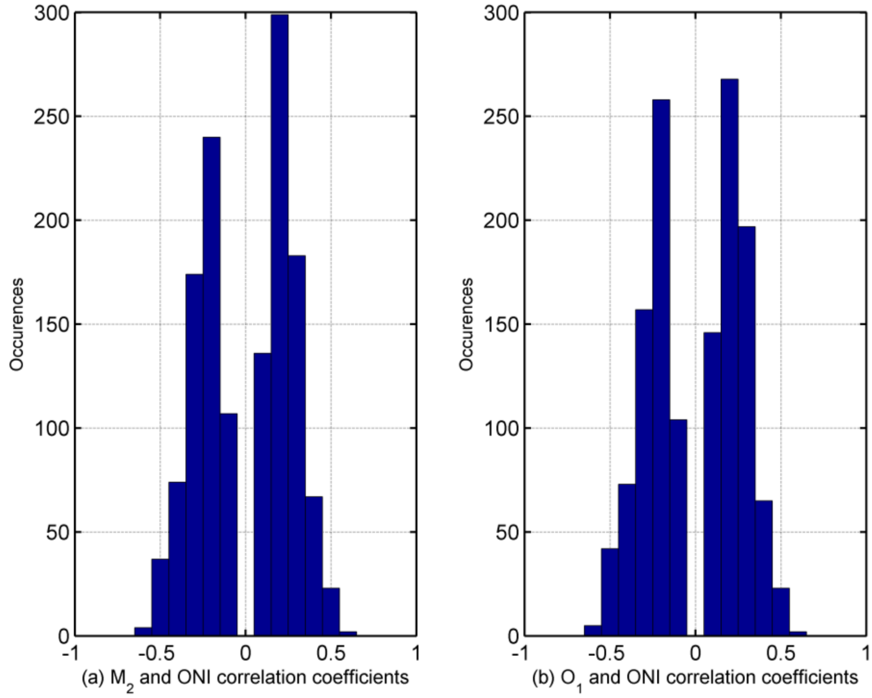

Figure 10. (a) Histogram of M_2 amplitudes and Oceanic Niño Index (ONI) correlation coefficients in the central deep basin of the SCS. (b) same as (a), but for O_1 amplitudes.

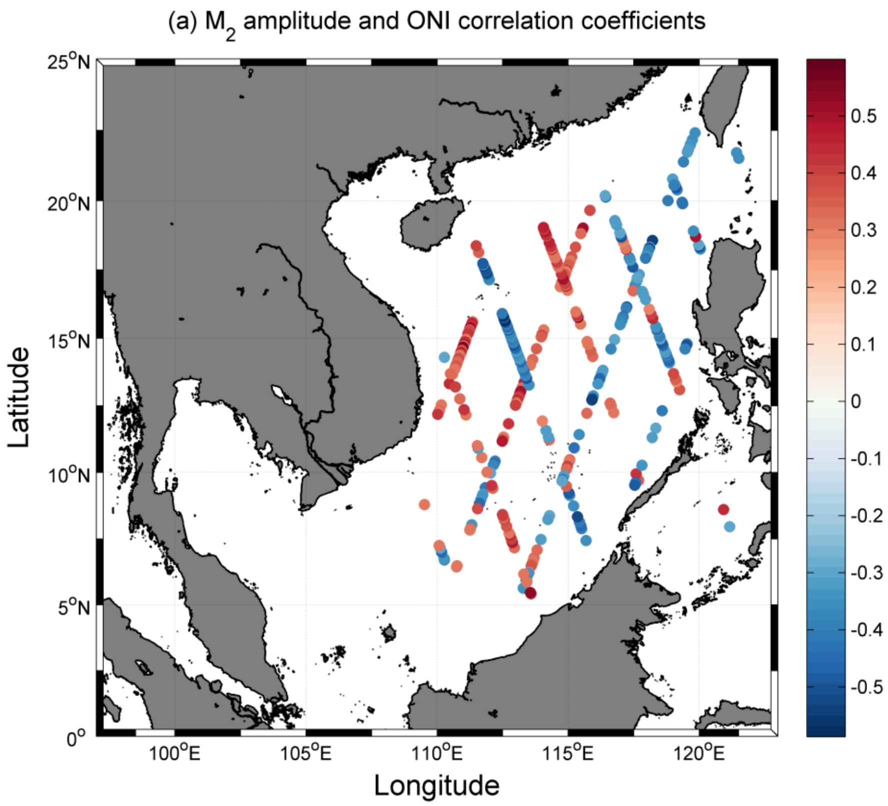

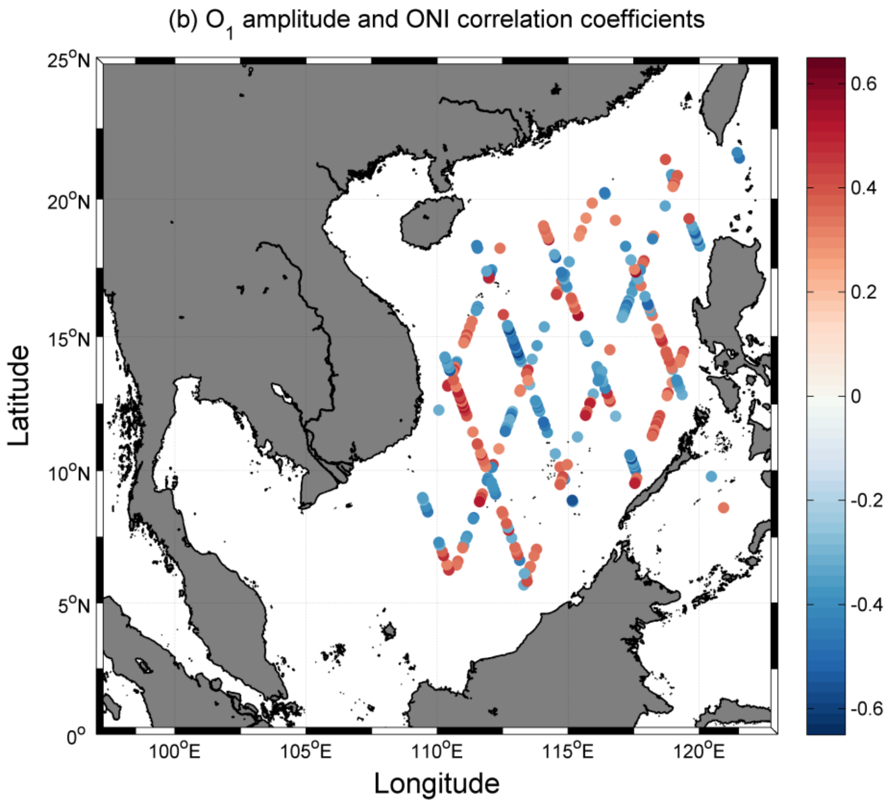

Figure 11. (a) The correlation coefficients between M_2 amplitudes and the Oceanic Niño Index (ONI) in the central deep basin of the SCS. (b) Same as (a), but for O_1 amplitudes. Only the positions where absolute correlation coefficients exceed 0.3 are displayed.

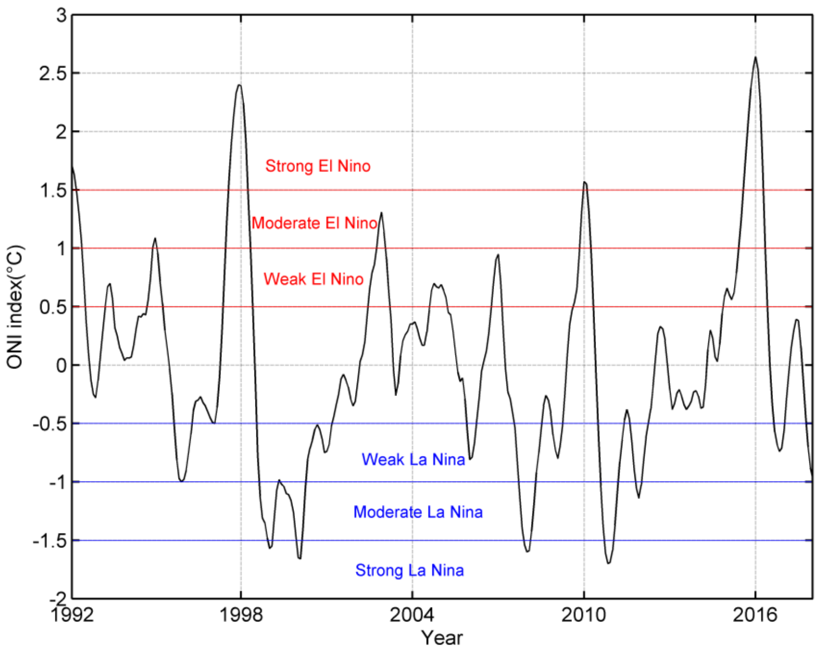

Figure 12. Oceanic Niño Index (ONI) from 1992 to 2017. The ONI uses the same region as the Niño 3.4 index (5N-5S, 170W-120W). To be classified as a full-fledged El Niño or La Niña, the sea surface temperature anomalies must exceed +0.5° C or -0.5° C for at least five consecutive months.

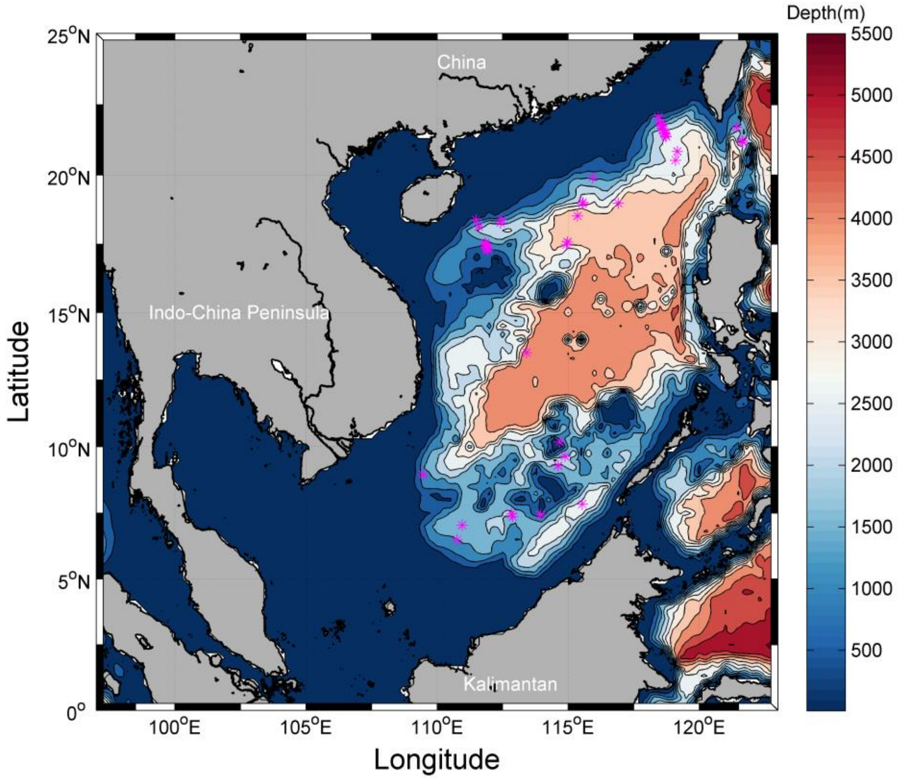

Figure 13. The positions (labeled by pink asterisks) where absolute M_2 and O_1 TACs exceed 300mm/m.

4.3.2 Limitations of the present study

Godin (1995) reported the rapid evolution of M_2 tides in the Gulf of Maine. At Eastport in the Gulf of Maine, the linear trend of M_2 amplitudes can be up to 13.7 ± 1.2cm/century, which is one of the largest linear tidal trends in the world (Ray 2006, Ray and Talke, 2019). However, in some regions in the SCS, the trends of K_1 amplitudes may be up to -0.153 ± 0.026cm/yr or -15.3 ± 2.6cm/century, which is an even larger magnitude than that seen in the Gulf of Maine. It should be noted that is the trends determined here are obtained from 25-year observations while is the observations in the Gulf of Maine were obtained from 50-year observations. Also, due to the long sampling period, the errors of the trends obtained from satellite data are significantly larger than those obtained from tide gauges. Therefore, it is clear that the trends as well as the inter-annual and decadal tidal variability obtained from relatively short satellite data are less stable and accurate than those obtained from hourly long-term tidal gauge observations.

Although there are hundreds of tide gauges in the global ocean, most of them were established after the 1980s and many of them are poorly maintained. Nearly all available long-term (more than 50 years) tide gauges are located on the coasts of Japan, North America, Australia, and Europe. For the tide gauges analyzed in this paper, both the location, number and time span are highly limited which hinders us from revealing possible coherent basin-wide patterns of tidal variability in the SCS. Most tide gauges (21 out of 24) are located on the coasts of Malaysia and China. There are almost no continuous long-term (more than 18.61 years) tide gauges in the coasts of Thailand and Vietnam although they have very long coastlines. Additionally, all observations at tide gauges provided by China are all outdated, with the exception of Hong Kong and Kaohsiung. Recent high-frequency (daily or hourly) water level observations are not publicly available because of concerns of security and propriety, and only limited monthly or yearly averaged data are accessible for scientific research.

5. Conclusion and Summary

Careful analysis of time-varying tidal characteristics is helpful and necessary for many practical purposes, such as navigation, coastal engineering, the utilization of tidal energy and flood prevention. It is common knowledge that ocean tides are changing in the global ocean based on long-term tide gauge observations. Less known, and less studied, is the tidal variability in the deep ocean where few tide gauges exist. In this paper, assisted by the novel methods of the S_TIDE toolbox and the TAC method, we analyzed the inter-annual and decadal tidal variability in the SCS using the combination of 25-year T/P-Jason satellite altimeter records and 24 coastal tide gauges. We found that for M_2 and O_1 constituents, about 17 IPs are suitable for S_TIDE to obtain inter-annual and decadal tidal variability in the SCS derived from satellite altimetry data, through an exhaustive amount of sensitivity experiments. For the rest of the constituents, we use 2 IPs in S_TIDE to extract the trends of tidal amplitudes. It is noted that the IP number suitable for extracting inter-annual and decadal tidal variability may vary with study regions and LOR. Therefore, the effective use of S_TIDE needs sensitivity experiments where IP numbers are varied to determine the optimal IP number in each region of interest.

For coastal tide gauges, we have emphasized the importance of completely removing the nodal modulations to improve the accuracy of the estimation of TACs. It is found that tidal variability and sea level variability are strongly correlated at inter-annual time scale at most positions in the SCS. The tides are likely influenced by sea level variations in coastal areas while in the deep water both mean sea level and tidal properties are likely influenced by ENSO. It is also found that the tides in the central deep basin of the SCS have significant and often large long-term trends.

The results obtained from satellite data are less stable and accurate than those obtained from long-term tide gauge records. However, the methods presented here provide an important supplement to the observed variability seen at coastal tide gauges, which are limited in time and space in the SCS region. As time goes by, the accuracy of satellite altimeter records will be improved and their length or record will increase, which will improve estimates. Additionally, next-generation altimetry missions, such as the recently launched Sentinel-6 mission from ESA (http://www.esa.int/Applications/Observing_the_Earth/Copernicus/Sentinel-6), and the upcoming Surface Water Ocean Topography (SWOT) platform from NASA (https://eospso.nasa.gov/missions/surface-water-ocean-topography) will bring new and improved observations of the coastal ocean, which will further help to resolve interannual variability behavior of sea level and tides and close the gap between coastal tide gauge observations and open-ocean altimetry observations.

Author Contributions

HP did all analyses, figures, tables, the majority of writing, and complied the manuscript. ATD and XL provided editing, insight, guidance, and direction to this study.

Competing Interests

The authors declare they have no competing interests.

Acknowledgements

The satellite altimeter data used in our study is downloaded from the Radar Altimeter Database System (http://rads.tudelft.nl/rads/rads.shtml). The tide gauge data used in our study is obtained from University of Hawaii Sea Level Center (https://uhslc.soest.hawaii.edu/). The filtered sea level anomaly (SLA) products can be obtained by request from Edward D. Zaron (Edward.D.Zaron@oregonstate.edu) or downloaded from the following website (https://drive.google.com/open?id=1cu3k_1Vjq_DdVGYvA5FRG70VXyUp_ngI). Oceanic Niño Index (ONI) is provided by National Center for Atmospheric Research (NCAR)(https://climatedataguide.ucar.edu/climate-data/nino-sst-indices-nino-12-3-34-4-oni-and-tni). The authors thank Rich Pawlowicz, Bob Beardsley, and Steve Lentz for providing the T_TIDE package. This research was funded by the National Natural Science Foundation of China (Grant No. 42076011 and Grant No.U1806214), the National Key Research and Development Program of China (Grant No. 2019YFC1408405).

S_TIDE v1.19 toolbox can be downloaded from https://www.researchgate.net/project/A-non-stationary-tidal-analysis-toolbox-S-TIDE. Eq.(4) is realized by s_tide_m4 function in S_TIDE toolbox.

Appendix A: Sensitivity experiments for determining optimal IP number

We performed a series of sensitivity experiments, where the IP number applied to the M_2 and O_1 tides increased gradually from 1 to 20 (the IP number for the rest constituents is set to 2). The IP number for MWL is set to 1 because sea level variability is removed via a prior correction described in Zaron and Ray (2018). There are 1600 T/P-Jason satellite observation positions in the SCS, and we use the results at 15.33°N, 118.38°E as an example (Figure A1). As the IP number increases, the performance of S_TIDE improves (Figure A2). When using only 1 IP, the hindcast of S_TIDE explains 96.07% of the original signal variance, with a root-mean-square error (RMSE) of 5.75cm and a maximum absolute error (MAE) of 18.87cm. When using 20 IPs, the hindcast of S_TIDE explains 96.64 % of the original signal variance, with a RMSE of 5.32cm and a MAE of 17.95cm. Note that when using 1 IP for the M_2 and O_1 tides, there are 37 unknowns that need to be solved in S_TIDE. When using 20 IPs for M_2 and O_1 tides, there are 113 unknowns. It is not surprising that 113 parameters do a better job than 37 parameters in describing the same data. However, this success is realized at the expense of more computation time and lower signal-to-noise ratio (SNR) of the results (Figure A2). As shown by the red line in Figure A2, when using 20 IPs, the time-averaged SNR of the M_2 amplitude is the smallest (only 6.16). There are 884 sea level observations at 15.33° N, 118.38° E. If we remove the missing values, there are only 733 sea level observations. Although 113 is still much smaller than 733 which means that we can still solve for these unknowns via least squares fitting, the 95% confidence intervals of 113 unknowns are much larger than those of 37 unknowns. If we also want to extract the inter-annual and decadal variability of other constituents such as S_2 and N_2, it is obvious that more unknowns are needed. To control the total number of unknowns and obtain a relatively higher SNR, we only use 2 IPs to extract the linear trends of all constituents except M_2 and O_1 tide.

As shown in Figure A3, when using 1 IP, the M_2 amplitude obtained by S_TIDE is time-invariant. When using 2 IPs, the M_2 amplitude shows a non-linear trend. Note that the non-linearity is caused by the non-linear relationship between *A*, *B* and *h*, *g* (namely, Eq.(3)). When the number of IP increases to 8, the M_2 amplitude shows oscillations with period of 6~8 years (Figure A3). When the number of IP increases to 17, the M_2 amplitudes show oscillations with period of 2~4 years (Figure A4 and Figure 2). However, the errors of the M_2 amplitudes (dash lines in Figure A4) also increase as the number of IP increases (especially near the boundaries). To ensure the reliability of tidal amplitudes near the boundaries, the number of IPs must be strictly restricted. It is found that 17 IPs are suitable for M_2 tide at this position. As shown in Figure A5, the O_1 amplitude obtained by 17 IPs is also reliable. We found that 17 IPs are also suitable for other positions in the SCS.

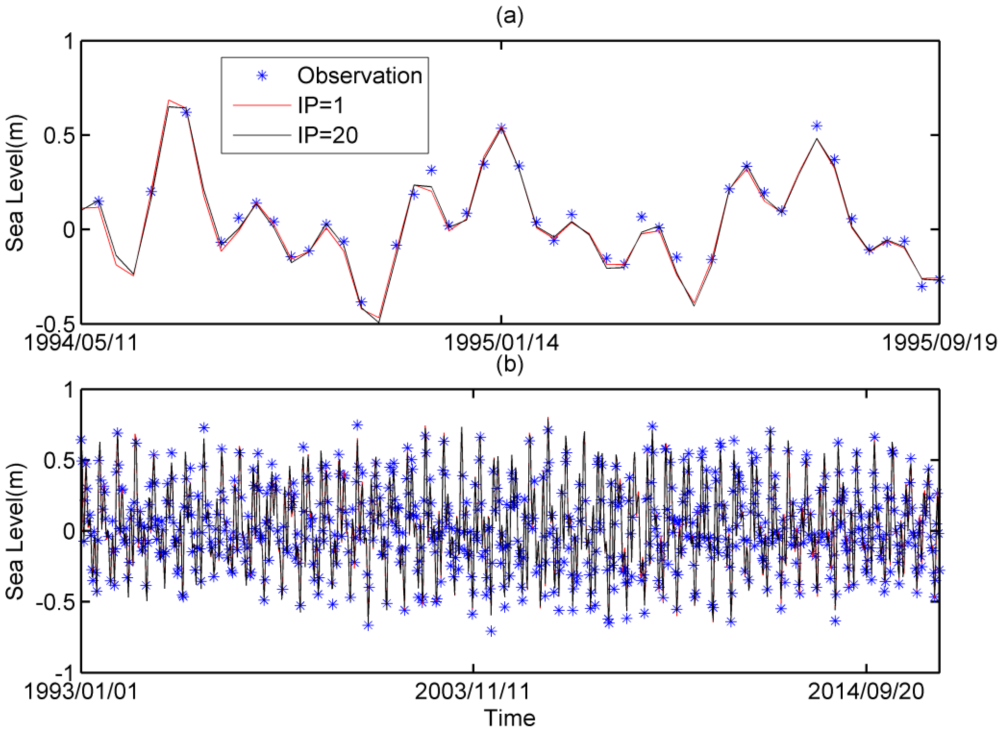

Figure A1. Sea level observations at 15.33° N, 118.38° E (blue dots) and the hindcast of S_TIDE obtained by 1 IP (red line) and 20 IPs (black line) (a) from 1994/05/01 to 1995/09/19 (b) from 1993/01/01 to 2016/09/23

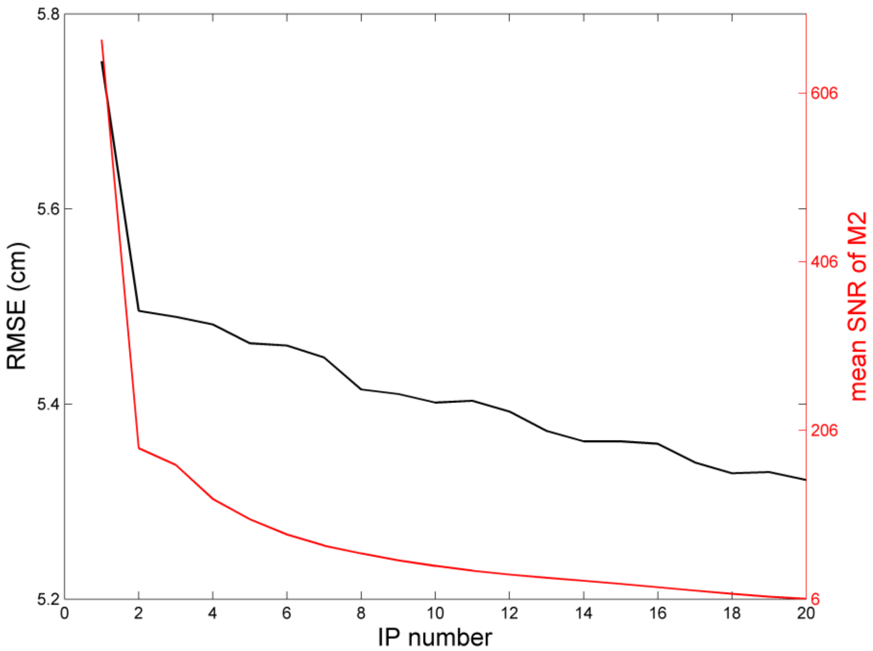

Figure A2. The root-mean-square error (RMSE) of the hindcast and time-averaged signal-to-noise rate (SNR) of M_2 amplitudes obtained by S_TIDE with different IPs at 15.33° N, 118.38° E.

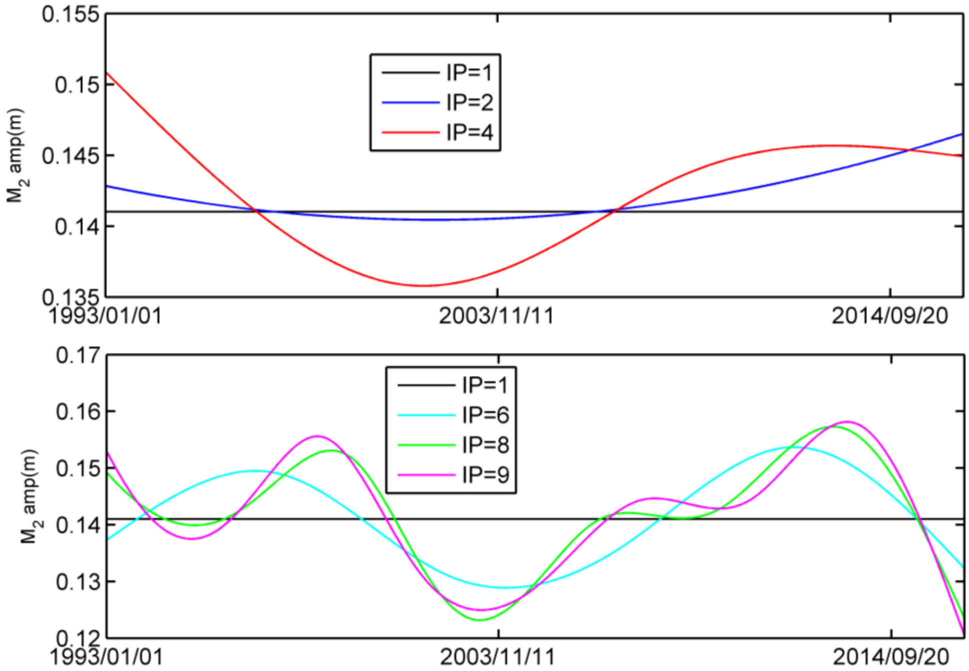

Figure A3. M_2 amplitudes obtained by S_TIDE using 1, 2, 4, 6, 8 and 9 IPs.

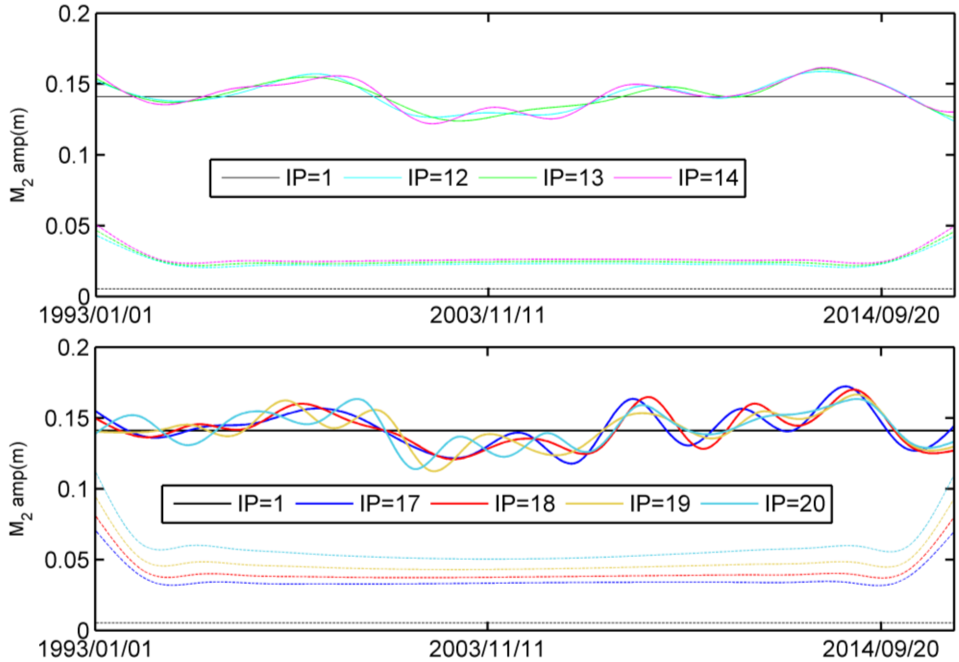

Figure A4. M_2 amplitudes obtained by S_TIDE using 1,12,13,14,17,18,19 and 20IPs (solid lines). Dashed lines are corresponding errors.

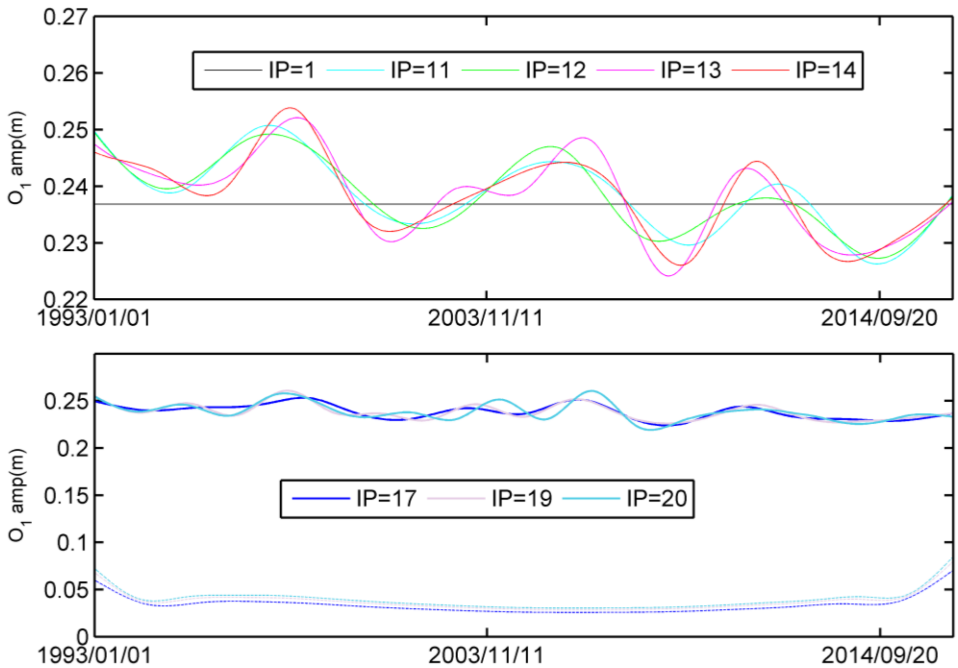

Figure A5. O_1 amplitudes obtained by S_TIDE using 1, 11, 12, 13,14,17,19 and 20 IPs (solid lines). Dashed lines are corresponding errors.

Appendix B:

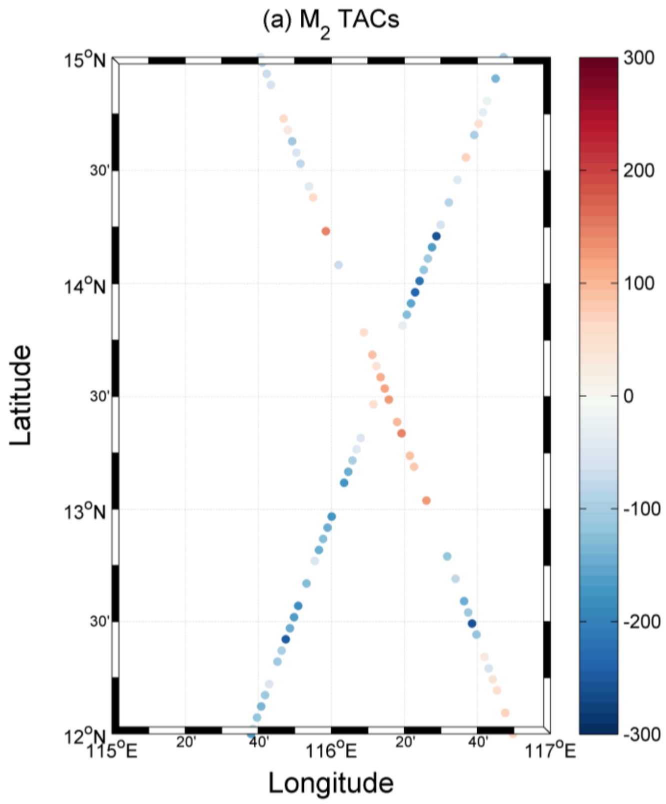

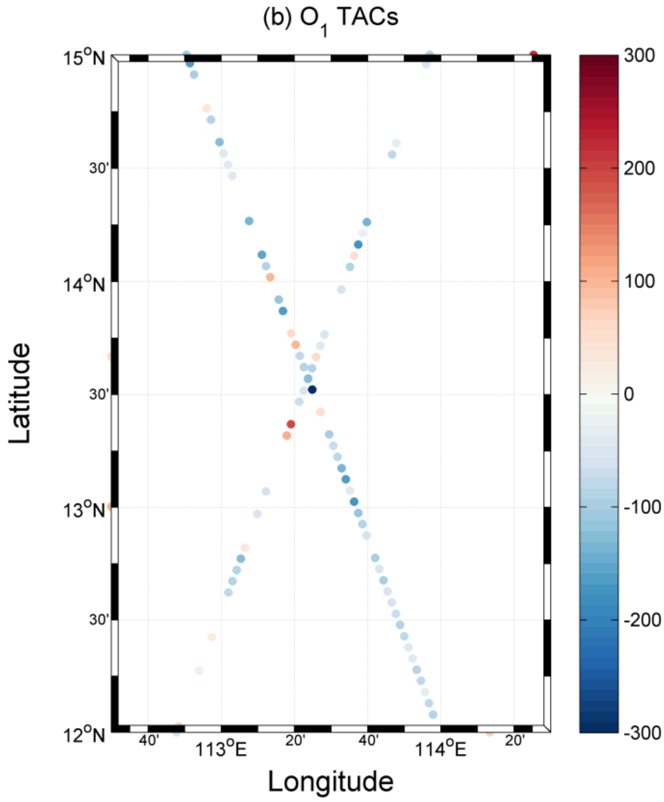

Figure B1. A zoomed-in version of Figure 6. Insignificant TACs are not displayed.

Reference

Alford, M. H. (2008), Observations of parametric subharmonic instability of the diurnal internal tide in the South China Sea. *Geophysical Research Letters*, 35, L15602.

Alford, M. H., MacKinnon, J. A., Nash, J. D., Simmons, H., Pickering, A., Klymak, J. M., Pinkel, R., Sun, O., Rainville, L., Musgrave, R., & Beitzel, T. (2011), Energy flux and dissipation in Luzon Strait: two tales of two ridges. *Journal of Physical Oceanography*, 41(11), 2211– 2222.

Amin, M. (1985), Temporal variations of tides on the west coast of Great Britain, *Geophysical Journal Royal Astronomical Society*, 82, 279–299.

Amin, M. (1993), Changing mean sea level and tidal constants on the west coast of Australia, *Marine Freshwater Research* , 44(6), 911–925.

Chant, R.J., C.K. Sommerfield, and S.A. Talke (2018), Impact of channel deepening on tidal and gravitational circulation in a highly engineered estuarine basin, *Estuaries Coasts*, 41, 1587–1600.

Cheng, X., S. Xie, Y. Du, Ji. Wang, X. Chen, and Ju. Wang (2015), Interannual-to-decadal variability and trends of sea level in the South China Sea, *Climate Dynamics*, 46, 1-14.

Colosi, J. A., and W. Munk (2006), Tales of the venerable Honolulu tide gauge, *J. Phys. Oceanogr.*, 36, 967–996.

Devlin, A. T., Jay, D. A., Talke, S. A., & Zaron, E. (2014), Can tidal perturbations associated with sea level variations in the western Pacific Ocean be used to understand future effects of tidal evolution? *Ocean Dynamics*, *64*(8), 1093–1120.

Devlin, A. T., Jay, D. A., Zaron, E. D., Talke, S. A., Pan, J., & Lin, H. (2017a)，Tidal variability related to sea level variability in the Pacific Ocean. *Journal of Geophysical Research: Oceans*, 122(11), 8445-8463.

Devlin, A. T., Jay, D. A., Talke, S. A., Zaron, E. D., Pan, J., & Lin, H. (2017b)，Coupling of sea level and tidal range changes, with implications for future water levels. *Scientific reports*, 7(1), 17021.

Devlin, A. T., Zaron, E. D., Jay, D. A., Talke, S. A., & Pan, J. (2018), Seasonality of

Tides in Southeast Asian Waters. *Journal of Physical Oceanography*, 48(50), 1169-1190.

Devlin, A. T., Pan, J., & Lin, H. (2019a), Extended spectral analysis of tidal variability in the North Atlantic Ocean. *Journal of Geophysical Research:Oceans, 124*, 506-526.

Devlin, A. T., Pan, J., & Lin, H. (2019b), Tidal variability in the Hong Kong region, *Ocean Science*, 15, 4, 853-864.

Devlin, A. T., Pan, J., & Lin, H. (2020), Multi-timescale analysis of tidal variability in the Indian Ocean using Ensemble Empirical Mode Decomposition. *Journal of Geophysical Research:Oceans*, 125(12), e2020JC016604.

Familkhalili, R., and S. A. Talke (2016), The effect of channel deepening on tides and storm surge: A case study of Wilmington, NC, *Geophys. Res. Lett.*, 43, 9138–9147.

Fang G, YK., Kwok, K.,Yu, and Y. Zhu (1999), Numerical simulation of principal tidal constituents in the South China Sea, Gulf of Tonkin, and Gulf of Thailand. *Continental Shelf Research* ,19(7),845–869.

Feng, X., M. N. Tsimplis, and P. L. Woodworth (2015), Nodal variations and long-term changes in the main tides on the coasts of China, *J. Geophys. Res. Oceans*, 120, 1215–1232.

Gao. X, Z. Wei, X. Lv,Y. Wang and G. Fang (2015), Numerical study of tidal dynamics in the South China Sea with adjoint method. *Ocean Modelling*, 92(2015),101-114.

Godin, G. (1995), Rapid evolution of the tide in the Bay of Fundy. *Continental Shelf Research*, 15, 369-372.

Green JAM, TW. David (2013), Non-assimilated tidal modeling of the South China Sea. *Deep-Sea Res PT I*, 78,42–48.

Jan, S., Chern, C. S., Wang, J., & Chao, S. Y. (2007), Generation of diurnal K1 internal tide in the Luzon Strait and its influence on surface tide in the South China Sea. *J. Geophys. Res. Oceans*, 112, C06019.

Jan, S., Lien, R. C., & Ting, C. H. (2008), Numerical study of baroclinic tides in Luzon Strait. *J. Oceanogr.*, 64(5), 789-802.

Jay, D. A. (2009), Evolution of tidal amplitudes in the eastern Pacific Ocean, *Geophys. Res. Lett.*, 36, L04603.

Jin, G., H. Pan, Q. Zhang, X. Lv, W. Zhao, and Y. Gao (2018), Determination of Harmonic Parameters with Temporal Variations: An Enhanced Harmonic Analysis Algorithm and Application to Internal Tidal Currents in the South China Sea, *J. Atmos. Ocean. Technol.*, 35(7), 1375-1398.

Ku, L.-F., Greenberg, D. A., Garrett, C. J. R., Dobson, F. W. (1985), Nodal modulation of the lunar semidiurnal tide in the Bay of Fundy and Gulf of Maine. *Science,* 230, 69-71.

Leffler, K. E., and D. A. Jay (2009), Enhancing tidal harmonic analysis: Robust (hybrid L1 / L2) solutions, *Cont. Shelf Res*., 29(1), 78–88.

Li, G., L. Cheng, J. Zhu, K.E. Trenberth, M.E. Mann, and J.P. Abraham (2020), Increasing ocean stratification over the past half-century, *Nat. Clim. Chang.*, 10(12), 1-8.

Lu, X., and J. Zhang (2006), Numerical study on spatially varying bottom friction coefficient of a 2D tidal model with adjoint method, *Cont. Shelf Res., 26(16)*, 1905–1923.

Matte, P., D. A. Jay, and E. D. Zaron (2013), Adaptation of Classical Tidal Harmonic Analysis to Nonstationary Tides, with Application to River Tides, *J. Atmos. Ocean. Technol.*, 30(3), 569–589.

Matte, P., Y. Secretan, and J. Morin (2014), Temporal and spatial variability of tidal-fluvial dynamics in the St. Lawrence fluvial estuary: An application of nonstationary tidal harmonic analysis, *J. Geophys. Res. Oceans*, 119, 5724–5744.

Mohan, S., P. Vethamony, and P. Tkalich (2015), Inter-annual sea level variability in the southern South China Sea, *Global and Planetary Change*, 133, 17-26.

Mohan, S., and P. Vethamony (2018), Interannual and long-term sea level variability in the eastern Indian Ocean and South China Sea, *Climate Dynamics*, 50, 1-23.

Mitchum, G. T., and S. M. Chriswell (2000), Coherence of internal tide variations along the Hawaiian Ridge. *Journal of Geophysical Research*,105, 28653-28661.

Müller, M. (2011), Rapid change in semi‐diurnal tides in the North Atlantic since 1980, *Geophys. Res. Lett.*, 38, L11602.

Pan, H., Z. Guo, and X. Lv (2017), Inversion of Tidal Open Boundary Conditions of the M2 Constituent in the Bohai and Yellow Seas, *J. Atmos. Oceanic Technol*, *34(8)*,1661-1672.

Pan, H., Z. Guo, Y. Wang, and X. Lv (2018a), Application of the EMD method to river tides. *J. Atmos. Oceanic Technol.*, 35(4), *809–819*.

Pan, H., X. Lv, Y. Wang, P. Matte, H. Chen, and G. Jin (2018b), Exploration of Tidal-Fluvial Interaction in the Columbia River Estuary Using S_TIDE, *J. Geophys. Res. Ocean.*, 123(9), 6598–6619.

Pan, H., and X. Lv (2019), Reconstruction of spatially continuous water levels in the Columbia River Estuary : The method of Empirical Orthogonal Function revisited, *Estuar. Coast. Shelf Sci.*, 222(April), 81–90.

Pan, H., Q. Zheng, and X. Lv (2019), Temporal changes in the response of the nodal modulation of the M_2 tide in the Gulf of Maine, *Cont. Shelf Res.*, 186(March), 13–20.

Pawlowicz, R., B. Beardsley, and S. Lentz (2002), Classical tidal harmonic analysis including error estimates in MATLAB using T_TIDE, Comput. Geosci., 28(8), 929–937.

Pelling, H. E. and J. A. M. Green (2013), Sea level rise and tidal power plants in the Gulf of Maine, *J. Geophys. Res.Oceans*, 118, 2863–2873.

Ralston, D.K., S. Talke, W.R. Geyer, H.A.M. Al-Zubaidi, C.K. Sommerfield (2019), Bigger tides, less flooding: Effects of dredging on barotropic dynamics in a highly modified estuary. *Journal of Geophysical Research Oceans*,124, 196–211.

Ray, R., and G. Michtum (1997), Surface manifestation of internal tides in the deep ocean: observations from altimetry and island gauges. *Progress in Oceanography*, 40, 135-162.

Ray, R. D. (1998), Spectral analysis of highly aliased sea-level signals. *J. Geophys. Res.*, 103(C11), 24, 991–25, 003.

Ray, R. D. (2006), Secular changes of the M2 tide in the Gulf of Maine, *Cont. Shelf Res.*, 26, 422–427.

Ray, R. D. (2009), Secular changes in the solar semidiurnal tide of the western North Atlantic Ocean, *Geophys. Res. Lett.*, 36, L19601.

Ray, R. D., and D. A. Byrne, (2010), Bottom pressure tides along a line in the southeast Atlantic Ocean and comparisons with satellite altimetry. *Ocean Dyn*., 60, 1167–1176.

Ray, R. D., and E. D. Zaron, (2016), Internal tides and their observed wavenumber spectra from satellite altimetry. *J. Phys. Oceanogr.*, 46, 3–22.

Ray, R. D. and Talke, S. A.(2019), Nineteenth-century tides in the Gulf of Maine and implications for secular trends, *J. Geophys. Res. Oceans*, 124,7046–7067.

Rong, Z.,Y., Liu, H., Zong, and Y. Cheng (2007), Interannual sea level variability in the South China Sea and its response to ENSO. *Global Planet Changes*, 55(4), 257– 272.

Simmons, H., Chang, M. H., Chang, Y. T., Chao, S. Y., Fringer, O., Jackson, C. R., & Ko, D. S. (2011), Modeling and prediction of internal waves in the South China

Sea. *Oceanography*, 24(4), 88– 99.

Stammer D., R. Ray, O. Andersen et al.(2014), Accuracy assessment of global barotropic ocean tide models. *Reviews of Geophysics*, 52, 243–282.

Wang, D., Wang, Q., Cai, S. et al. (2019), Advances in research of the mid-deep South China Sea circulation, *Sci. China Earth Sci.*, 62, 1992–2004.

Wang, D., H. Pan, G. Jin and X. Lv (2020), Seasonal variation of the main tidal constituents in the Bohai Bay, *Ocean Science*, 16,1-14.

Woodworth, P. L., S. M. Shaw, and D. L. Blackman (1991), Secular trends in mean tidal range around the British Isles and along the adjacent European coastline, *Geophys. J. Int.*, 104, 593–609.

Xie, X. H., Chen, G. Y., Shang, X. D., & Fang, W. D. (2008), Evolution of the semidiurnal (M2) internal tide on the continental slope of the northern South China Sea. *Geophys. Res. Lett.*, 35(13), L13604.

Xie, X. H., Shang, X. D., van Haren, H., Chen, G. Y., & Zhang, Y. Z. (2011), Observations of parametric subharmonic instability‐induced near‐inertial waves equatorward of the critical diurnal latitude. *Geophys. Res. Lett.*, 38(5), L05603.

Xie, X., Shang, X., Haren, H., & Chen, G. (2013), Observations of enhanced nonlinear instability in the surface reflection of internal tides. *Geophys. Res. Lett.*, 40(8), 1580-1586.

Zaron, E. D., and R. D.Ray (2018), Aliased tidal variability in mesoscale sea level anomaly maps. *J. Atmos. Oceanic Technol.*, 35(12),2421-2434.

Zaron, E. D. (2019), Baroclinic tidal sea level from exact-repeat mission altimetry. *Journal of Physical Oceanography*, 49(1),193-210.

Zhai, R., G. Chen, C. Liang, X. Shang, and J. Xie (2020), The influence of ENSO on the structure of internal tides in the Xisha area, *Journal of Geophysical Research:Oceans*, 125(3), e2019JC015405.

Zhang, N., J. Wang, Y. Wu, K.-H. Wang, Q. Zhang, S. Wu, Z.-J. You, and Y. Ma (2019), A modelling study of ice effect on tidal damping in the Bohai Sea, *Ocean Engineering*, 173, 748-760.

Zhang, Z., W. Zhao, J. Tian, and X. Liang (2013), A mesoscale eddy pair southwest of Taiwan and its influence on deep circulation, *J. Geophys. Res. Oceans*, 118, 6479– 6494.

Zhao, Z. X. (2016), Internal tide oceanic tomography. *Geophys. Res. Lett.*, 43, 9157–9164.

Zong, X., H. Pan, Y. Liu, and X. Lv (2018), Improved Estimation of Pollutant Emission Rate in an Ocean Pollutant Diffusion Model by the Application of Spline Interpolation with the Adjoint Method, *J. Atmos. Ocean. Technol.*, *35*(10), 1961–1975.

Zu T., J. Gan, and SY. Erofeeva (2008), Numerical study of the tide and tidal dynamics in the South China Sea, *Deep-Sea Res PT I*, 55(2),137–154.